

Hp Generalized FEM and crack surface representation for non-planar 3-D cracks *

J.P. Pereira[†], C.A. Duarte^{†,‡}, D. Guoy[‡], and X. Jiao^{††}

August 5, 2008

[†]*Department of Civil & Environmental Engineering,*

University of Illinois at Urbana-Champaign, 205 North Mathews Ave., Urbana, IL 61801, U.S.A..

[‡]*Center for Simulation of Advanced Rockets,*

University of Illinois at Urbana-Champaign, 1304 West Springfield Avenue, Urbana, IL 61801, U.S.A..

^{††}*Department of Applied Mathematics and Statistics, Stony Brook University, Stony Brook, NY 11794-3600.*

Abstract

A high-order generalized finite element method (GFEM) for non-planar three-dimensional crack surfaces is presented. Discontinuous p -hierarchical enrichment functions are applied to strongly graded tetrahedral meshes automatically created around crack fronts. The GFEM is able to model a crack arbitrarily located within a finite element mesh and thus the proposed method allows fully automated fracture analysis using an existing finite element discretization without cracks. We also propose a crack surface representation that is independent of the underlying GFEM discretization and controlled only by the physics of the problem. The representation preserves continuity of the crack surface while being able to represent non-planar, non-smooth, crack surfaces inside of elements of any size. The proposed representation also provides support for the implementation of accurate, robust and computationally efficient numerical integration of the weak form over elements cut by the crack surface. Numerical simulations using the proposed GFEM show high convergence rates of extracted stress intensity factors along non-planar curved crack fronts and the robustness of the method.

Keywords: Generalized finite element method; Extended finite element method; Fracture; High-order approximations.

1 Introduction

Crack growth prediction is of great importance in many areas of application, such as assessment of structural components subjected to extreme loading conditions and fatigue failure analysis. In these cases, engineering decisions must be based on accurate evaluation of crack front quantities such as energy release rate and stress intensity factors. These quantities are, in turn, dependent on the accuracy of the 3-D numerical

*Preprint of IJNME paper. DOI: 10.1002/nme.2419

[†]Corresponding author. E-mail: caduarte@uiuc.edu

analysis performed. However, accurate 3-D analysis of fracture mechanics problems is still a challenging task.

In a standard finite element analysis, it is well known that the combination of h - and p -extensions, the so-called hp -version [55], exhibits exponential convergence rates for fracture mechanics problems. However, the craft of optimal hp FEM discretizations for arbitrary 3-D crack problems is not a trivial task and is difficult to fully automate. It requires, in general, human intervention and thus leading to a costly analysis.

Partition of unity methods such as the GFEM [4, 11, 12, 15, 41, 51] and the XFEM [7, 37] are promising candidates to overcome the mesh design issues of the FEM. These methods greatly facilitate the modeling of arbitrary 3-D cracks since element faces are not required to fit the crack surfaces.

Early developments of p -hierarchical enrichment of arbitrary degree for the GFEM can be found in the works of Duarte et al. [41] and Taylor et al. [58]. In these references, the method is applied to 2-D linear elastic problems. P -hierarchical GFEMs for three-dimensional elasticity problems with edge-singularities were first proposed in [11, 12]. Quadratic XFEM approximations for 2-D fracture problems have been presented in Stazi et al. [50], Wells and Sluys [60], and Mariani and Perego [34]. Cubic approximations are discussed in the work of Laborde et al. [30]. Their high order approximations are based on non-hierarchical Lagrangian shape functions.

A GFEM for 3-D cracks was proposed by Duarte et al. [13, 14, 15] using a discontinuous partition of unity and enrichment functions built from high order polynomial and Westergaard near crack tip expansions. Early works on the XFEM for 3-D planar and non-planar crack surfaces using Heaviside step function and Westergaard functions include the works of Sukumar et al. [9, 52, 53] and Moës et al. [24, 38], respectively. More recent developments for 3-D crack analysis include the works of Areias and Belytschko [1], Gasser and Holzapfel [22], Mergheim et. al.[36], and Oliver et al. [43].

Duarte et al. [16] have proposed a high-order GFEM for through-the-thickness branched cracks in which the displacement field is enriched with high-order p -hierarchical GFEM approximations. They have consistently used high-order hierarchical GFEM approximations for single and multiple branched cracks that are planar through the thickness of the analysis domain. In their work, the concept of the so-called high-order step function is introduced. Their high-order enrichment functions are applied to the GFEM approximation using the partition of unity concept with linear FE shape functions. A brief comparison between Lagrangian and p -hierarchical GFEM enrichments is presented in [16].

This paper presents an hp -extension of the generalized finite element method (GFEM) for non-planar 3-D crack surfaces. Using the ease of creation of high-order enrichment functions and the ability of the GFEM to model a crack arbitrarily located within a finite element mesh, we are able to show that the proposed hp -GFEM can provide accurate solutions and high convergence rates for stress intensity factors of 3-D fracture mechanics problems.

H -refinements can be easily applied in the GFEM since the volume mesh need not fit the geometrical representation of crack surfaces. This greatly facilitates the construction of strongly graded meshes in the neighborhood of crack fronts while preserving the aspect ratio of the elements. The proposed discretization process applies p -hierarchical enrichment to meshes strongly graded around 3-D crack fronts. Both the p -enrichment and the h -refinement are fully automated, and thus the proposed hp methodology can be applied to initial finite element meshes that are arbitrarily coarse. The proposed enrichment for nodes near the crack front is based on the Westergaard expansion of the elasticity solution near a crack front. They allow modeling of crack fronts located inside elements and not necessarily at their boundary.

The p -hierarchical enrichment developed here is an extension of the approach presented in [16] to the case of non-planar 3-D crack surfaces. The high-order continuous and discontinuous approximations

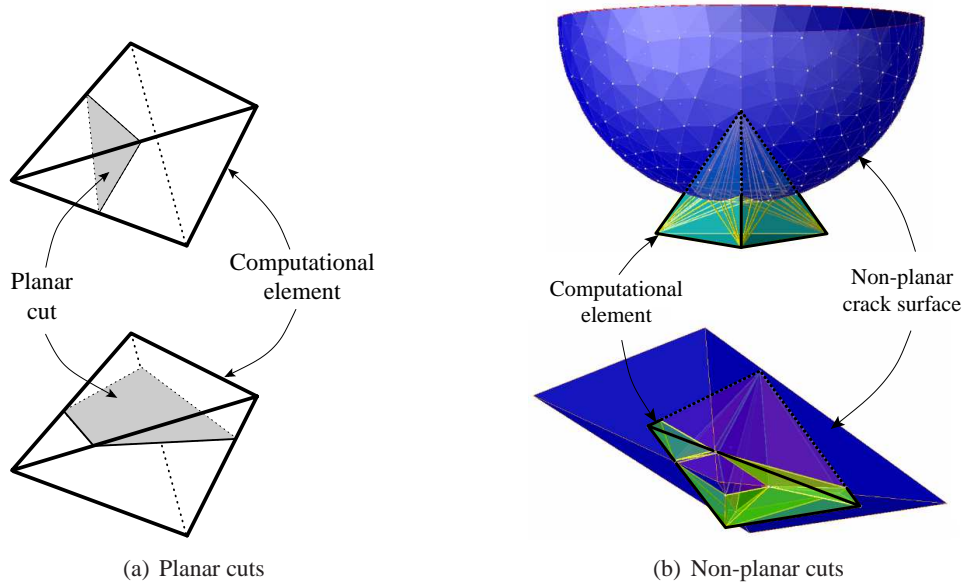


Figure 1: Examples of elements cut by a crack surface. Each figure shows a single computational element and different planar and non-planar cuts. Sub-elements used to integrate the weak form are also shown in Figure (b). Details on these sub-elements are presented in Section 4.2.

are able to deliver optimal convergence rates. The theoretical formulation of our approach is presented in Section 3.

Numerical examples demonstrating the flexibility and robustness of the proposed method are presented. We show that the proposed GFEM enables fully automated simulations of fracture mechanics problems of industrial level complexity.

Optimal hp -discretizations of fracture mechanics problems use strongly graded meshes and low-order approximations near crack fronts and large, high-order, elements away from singularities [55]. Thus, optimal hp -GFEM discretizations may have large elements cut by a crack surface since, in this class of methods, a crack may be arbitrarily located within a finite element, as illustrated in Figures 1 and 9. The geometrical representation of a crack surface must, therefore, be capable of handling 3-D non-planar crack surfaces inside an element. In addition, the surface may be non-smooth inside an element in order to represent sharp turns in a crack propagation simulation (Cf. Figure 10(c)).

Commonly used crack surface representations assume, in general, that the surface is planar inside an element [1, 21, 22, 36]. Thus, the actual surface is approximated by an average plane inside each element. While this greatly facilitates the computational implementation, it may also lead to several issues even when relatively small, low-order, elements are used. According to [1, 22, 36], the use of the planar-cut approach in a mixed-mode crack growth simulation, may lead to discontinuous crack surfaces along the boundary between elements. Proposed remedies for this require modifications to the crack surface in order to enforce continuity. Thus, the crack surfaces actually used in the computations are biased by the underlying meshes, like in the FEM. Ideally, the crack surface geometry should be based only on the governing physics of the problem, regardless of the discretization used for the field variables. The limitations of planar-cut representations can be ameliorated by using finer finite element meshes along the crack surface. However, this coupling between crack surface representation and problem discretization may substantially increase the computational cost of problems with complex crack surfaces. This coupling also exists in methods

that use the finite element mesh to define implicit representations of crack surfaces based on, for example, level sets [47]. If linear finite elements are used to represent the level set function, the crack surface is also planar inside each element. However, in this case, the level set function provides a continuous, albeit approximated, crack surface representation. Level sets are broadly used in the eXtended finite element method [24, 38, 53]. A review of level set techniques applied to crack surface representations can be found in [19].

In this paper, we propose a crack surface representation that is independent of the underlying GFEM discretization. It is based on an explicit 3-D surface triangulation of the crack surface, like in the approaches proposed in [1, 15, 21, 22, 29]. It provides consistent representation of non-planar non-smooth crack surfaces inside of elements of any size, while preserving its continuity. Explicit crack surface representations are also convenient to represent branched crack surfaces [16] and facilitate the visualization of crack surfaces using standard graphical post-processors. Details on the proposed approach are presented in Section 4.

Some examples to numerically verify the approach proposed in this paper are presented in Section 5. The level of refinement and the polynomial degree required in the approximation for a given level of accuracy is discussed in the numerical examples. Moreover, the robustness of the present approach in solving problems of increasing level of complexity is also verified in the subsequent sections. The *hp*-GFEM shows high convergence rates and accurate results for energy norm as well as for extraction of stress intensity factors in arbitrary 3-D crack surface problems.

2 Problem formulation

In this paper, we analyze three dimensional fracture mechanics problems assuming linear elastic isotropic material behavior. This section presents the weak and strong formulations for this kind of problem. However, the discrete formulation presented in Section 4 is not limited to the type of problem presented in this section.

2.1 Strong form

Consider a three dimensional domain Ω with boundary $\partial\Omega$ as illustrated in Figure 2. The domain boundary is subdivided into Γ^u , Γ^t , and Γ^c . Displacements are prescribed in Γ^u and tractions are prescribed in both Γ^t and Γ^c . Γ^c represents the crack surface.

For the sake of simplifying the notation, the formulation presented here is based on a single crack surface with one crack front only. However, the procedure can be easily extended to several cracks and to cracks with multiple fronts as well.

The equilibrium equations, constitutive relations and kinematic equations are given by

$$\begin{aligned}\nabla \cdot \boldsymbol{\sigma} + \mathbf{b} &= \mathbf{0} \quad \text{in } \Omega \\ \boldsymbol{\sigma} &= \mathbf{C} : \boldsymbol{\varepsilon} \\ \boldsymbol{\varepsilon} &= \nabla_s \mathbf{u}\end{aligned}\tag{1}$$

where $\boldsymbol{\sigma}$ is the Cauchy stress tensor, \mathbf{b} are body forces, $\boldsymbol{\varepsilon}$ is the linear strain tensor, ∇_s is the symmetric part of the gradient operator and \mathbf{C} is the Hooke's tensor. The boundary conditions are prescribed in $\partial\Omega$ as follows

$$\begin{aligned}
\mathbf{u} &= \bar{\mathbf{u}} \quad \text{on } \Gamma^u \\
\boldsymbol{\sigma} \cdot \mathbf{n} &= \bar{\mathbf{t}} \quad \text{on } \Gamma^t \\
\boldsymbol{\sigma} \cdot \mathbf{n} &= \bar{\mathbf{t}}_c \quad \text{on } \Gamma^c
\end{aligned}$$

where \mathbf{n} is an outward unit normal vector on $\partial\Omega$ and $\bar{\mathbf{u}}$, $\bar{\mathbf{t}}$, and $\bar{\mathbf{t}}_c$ are prescribed displacements and tractions, respectively.

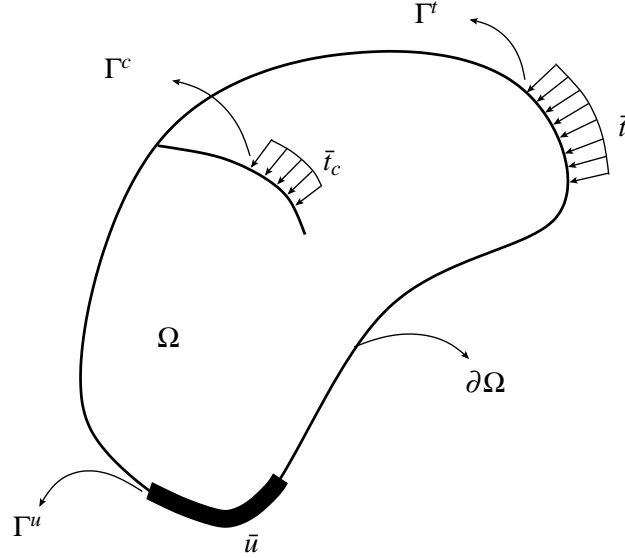


Figure 2: Three-dimensional boundary value problem.

2.2 Weak form

Let the set of kinematically admissible displacement fields be

$$\tilde{H}^1(\Omega) = \{\mathbf{u} \mid \mathbf{u} \in H^1(\Omega), \mathbf{u} = \bar{\mathbf{u}} \text{ on } \Gamma^u\}$$

where H^1 is the Hilbert space.

Let the set of virtual kinematically admissible displacement fields be

$$\overset{o}{H}^1(\Omega) = \{\mathbf{v} \mid \mathbf{v} \in H^1(\Omega), \mathbf{v} = \mathbf{0} \text{ on } \Gamma^u\}$$

The weak form of the equilibrium equations can be stated as follows.

$$\begin{aligned}
&\text{Find } \mathbf{u} \in \tilde{H}^1(\Omega) \text{ such that} \\
&B(\mathbf{u}, \mathbf{v}) = L(\mathbf{v}) \quad \forall \mathbf{v} \in \overset{o}{H}^1
\end{aligned}$$

where $B(\cdot, \cdot)$ and $L(\cdot)$ are the bilinear and linear forms, respectively, and are given by

$$B(\mathbf{u}, \mathbf{v}) = \int_{\Omega} \boldsymbol{\sigma}^{(\mathbf{u})} : \boldsymbol{\epsilon}^{(\mathbf{v})} d\Omega$$

$$L(\mathbf{v}) = \int_{\Omega} \mathbf{b} \cdot \mathbf{v} d\Omega + \int_{\Gamma^t} \bar{\mathbf{t}} \cdot \mathbf{v} d\Gamma + \int_{\Gamma^c} \bar{\mathbf{t}}_c \cdot \mathbf{v} d\Gamma$$

Let us now consider the case of a Cauchy or spring boundary condition, $\bar{\mathbf{t}}_s$, applied on Γ^s and given by

$$\boldsymbol{\kappa}(\boldsymbol{\delta}_s - \mathbf{u}) = \bar{\mathbf{t}}_s$$

where $\boldsymbol{\kappa}$ is the constitutive tensor of the spring system, $\boldsymbol{\delta}_s$ is the prescribed displacement at the base of the spring system. In the weak form, this type of boundary condition is added to the linear form as follows.

$$\int_{\Gamma^s} \bar{\mathbf{t}}_s \cdot \mathbf{v} d\Gamma = \int_{\Gamma^s} \boldsymbol{\kappa}(\boldsymbol{\delta}_s - \mathbf{u}) \cdot \mathbf{v} d\Gamma \quad (2)$$

In the limit case, any type of boundary condition can be written in terms of Cauchy boundary condition [55]. The penalty method, for example, corresponds to the case in which the stiffness of the spring is much larger than the stiffness of the body. Dirichlet boundary conditions can then be enforced by setting $\kappa_{ij} = 0$ if $i \neq j$ and $\kappa_{ij} = \eta$ if $i = j$, $\boldsymbol{\delta}_s = \bar{\mathbf{u}}$, and $\Gamma^s = \Gamma^u$. Thus, Equation (2) can be rewritten as follows

$$\int_{\Gamma^u} \eta \mathbf{I}(\bar{\mathbf{u}} - \mathbf{u}) \cdot \mathbf{v} d\Gamma = \eta \int_{\Gamma^u} \bar{\mathbf{u}} \cdot \mathbf{v} d\Gamma - \eta \int_{\Gamma^u} \mathbf{u} \cdot \mathbf{v} d\Gamma$$

The weak form is restated as

$$\text{Find } \mathbf{u} \in H^1(\Omega) \text{ such that}$$

$$B(\mathbf{u}, \mathbf{v}) = L(\mathbf{v}) \quad \forall \mathbf{v} \in H^1$$

where

$$B(\mathbf{u}, \mathbf{v}) = \int_{\Omega} \boldsymbol{\sigma}^{(\mathbf{u})} : \boldsymbol{\epsilon}^{(\mathbf{v})} d\Omega + \eta \int_{\Gamma^u} \mathbf{u} \cdot \mathbf{v} d\Gamma$$

$$L(\mathbf{v}) = \int_{\Omega} \mathbf{b} \cdot \mathbf{v} d\Omega + \int_{\Gamma^t} \bar{\mathbf{t}} \cdot \mathbf{v} d\Gamma + \int_{\Gamma^c} \bar{\mathbf{t}}_c \cdot \mathbf{v} d\Gamma + \eta \int_{\Gamma^u} \bar{\mathbf{u}} \cdot \mathbf{v} d\Gamma$$

The penalty formulation is attractive from the implementation point of view because it does not require, for example, that the shape functions have the Kronecker delta property. The penalty number, however, must be chosen with care. In the numerical examples presented in this paper, the penalty number is taken as $\eta = 10^8 * E * J$, where E and J are the Young's modulus of the material and the Jacobian of a volume element with a face on Γ^u , respectively. Theoretical analysis of the penalty method for the GFEM is presented in [2]. Other methods, like the Nitsche method or the Characteristic function method could be used as well. Details on these and other methods, as well as their theoretical analysis, is presented in the survey paper by Babuska et al. [2].

3 High Order GFEM for Arbitrary 3-D Cracks

This section discusses the discretization of the weak form presented in Section 2.2. We show the selection of enrichment functions that fit the goals of the *hp*-GFEM discretization.

3.1 GFEM—A Brief Overview

The generalized FEM [4, 12, 35, 41, 51] is an instance of the so-called partition of unity method [3, 17, 18]. It adds to the classical FEM some of the flexibility enjoyed by meshfree methods [2, 8, 25, 32, 33]. The GFEM can be regarded as a FEM with shape functions built using the concept of a partition of unity. In the GFEM considered here, a shape function $\phi_{\alpha i}$ is built from the product of a linear finite element shape function, φ_α , and an enrichment function, $L_{\alpha i}$,

$$\phi_{\alpha i}(\mathbf{x}) = \varphi_\alpha(\mathbf{x})L_{\alpha i}(\mathbf{x}) \quad (\text{no summation on } \alpha) \quad (3)$$

where α is a node in the finite element mesh. Figure 3 illustrates the construction of GFEM shape functions using a polynomial enrichment function.

The linear finite element shape functions φ_α , $\alpha = 1, \dots, N$, in a finite element mesh with N nodes constitute a partition of unity, i.e., $\sum_{\alpha=1}^N \varphi_\alpha(\mathbf{x}) = 1$ for all \mathbf{x} in a domain Ω covered by the finite element mesh. This is a key property used in partition of unity methods.

Several enrichment functions can be hierarchically added to any node α in a finite element mesh. Thus, if D_L is the number of enrichment functions at node α , the GFEM approximation, \mathbf{u}^{hp} , of a function \mathbf{u} can be written as

$$\begin{aligned} \mathbf{u}^{hp}(\mathbf{x}) &= \sum_{\alpha=1}^N \sum_{i=1}^{D_L} \underline{\mathbf{u}}_{\alpha i} \phi_{\alpha i}(\mathbf{x}) = \sum_{\alpha=1}^N \sum_{i=1}^{D_L} \underline{\mathbf{u}}_{\alpha i} \varphi_\alpha(\mathbf{x}) L_{\alpha i}(\mathbf{x}) \\ &= \sum_{\alpha=1}^N \varphi_\alpha(\mathbf{x}) \sum_{i=1}^{D_L} \underline{\mathbf{u}}_{\alpha i} L_{\alpha i}(\mathbf{x}) = \sum_{\alpha=1}^N \varphi_\alpha(\mathbf{x}) \mathbf{u}_\alpha^{hp}(\mathbf{x}) \end{aligned}$$

where $\underline{\mathbf{u}}_{\alpha i}$, $\alpha = 1, \dots, N$, $i = 1, \dots, D_L$, are nodal degrees of freedom and $\mathbf{u}_\alpha^{hp}(\mathbf{x})$ is a local approximation of \mathbf{u} defined on $\omega_\alpha = \{\mathbf{x} \in \Omega : \varphi_\alpha(\mathbf{x}) \neq 0\}$, the support of the partition of unity function φ_α . In the case of a finite element partition of unity, the support ω_α (often called cloud) is given by the union of the finite elements sharing a vertex node \mathbf{x}_α [12]. The equation above shows that the global approximation $\mathbf{u}^{hp}(\mathbf{x})$ is built by pasting together local approximations \mathbf{u}_α^{hp} , $\alpha = 1, \dots, N$, using a partition of unity. This is a concept common to all partition of unity methods.

The local approximations \mathbf{u}_α^{hp} , $\alpha = 1, \dots, N$, belong to local spaces $\chi_\alpha(\omega_\alpha) = \text{span}\{L_{i\alpha}\}_{i=1}^{D_L}$ defined on the supports ω_α , $\alpha = 1, \dots, N$. The selection of the enrichment or basis functions for a particular local space $\chi_\alpha(\omega_\alpha)$ depends on the local behavior of the function \mathbf{u} over the cloud ω_α . In the case of the fracture mechanics problem described in Section 2.1, the elasticity solution \mathbf{u} may be written as

$$\mathbf{u} = \hat{\mathbf{u}} + \tilde{\mathbf{u}} + \check{\mathbf{u}} \quad (4)$$

where $\hat{\mathbf{u}}$ is a continuous function, $\tilde{\mathbf{u}}$ is a discontinuous function but non-singular and $\check{\mathbf{u}}$ is a discontinuous and singular function. This *a priori* knowledge about the solution \mathbf{u} is used below to select basis functions for a local space $\chi_\alpha(\omega_\alpha)$.

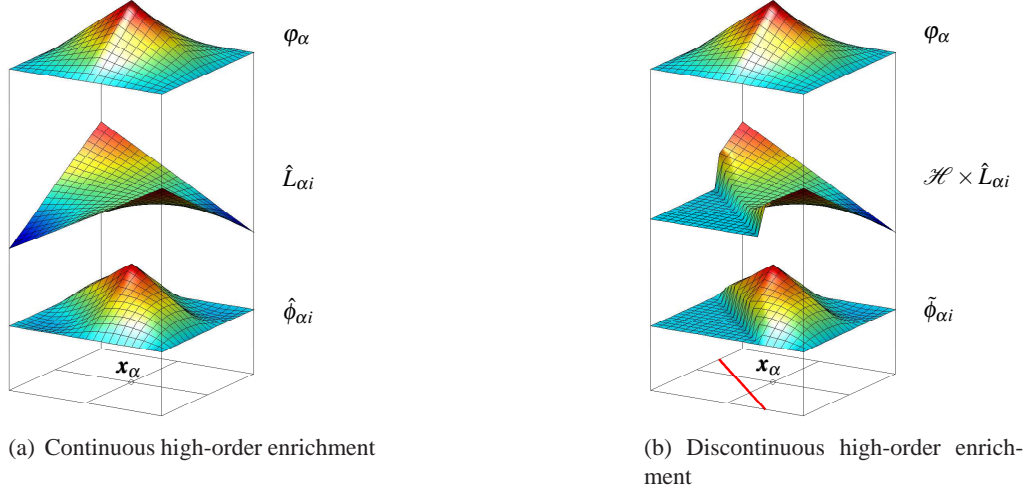


Figure 3: Construction of a GFEM shape function using a polynomial enrichment. Here, φ_α is the function at the top, the enrichment function, $\hat{L}_{\alpha i}$, is the function in the middle, and the generalized FE shape function, $\hat{\phi}_{\alpha i}$, is the resulting bottom function.

3.2 Enrichment Functions

In this section, we select the enrichment functions used to build the GFEM shape functions defined in (3). These functions, in turn, are basis functions for local spaces $\chi_\alpha(\omega_\alpha)$, $\alpha = 1, \dots, N$.

Local approximation for a continuous function Let ω_α denote a cloud such that the elasticity solution, \mathbf{u} , is continuous over ω_α . A local approximation, $\hat{\mathbf{u}}_\alpha^{hp}(\mathbf{x})$, of \mathbf{u} over ω_α can be written as

$$\hat{\mathbf{u}}_\alpha^{hp}(\mathbf{x}) = \sum_{i=1}^{\hat{D}_L} \hat{\mathbf{u}}_{\alpha i} \hat{L}_{\alpha i}(\mathbf{x})$$

where \hat{D}_L is the dimension of a set of polynomial enrichment functions of degree less than or equal to $p-1$. Our implementation follows [12, 41] and the set $\{\hat{L}_{\alpha i}\}_{i=1}^{\hat{D}_L}$ for a cloud associated with node $\mathbf{x}_\alpha = (x_\alpha, y_\alpha, z_\alpha)$ is given by

$$\{\hat{L}_{\alpha i}\}_{i=1}^{\hat{D}_L} = \left\{ 1, \frac{(x-x_\alpha)}{h_\alpha}, \frac{(y-y_\alpha)}{h_\alpha}, \frac{(z-z_\alpha)}{h_\alpha}, \frac{(x-x_\alpha)^2}{h_\alpha^2}, \frac{(y-y_\alpha)^2}{h_\alpha^2}, \dots \right\} \quad (5)$$

with h_α being a scaling factor [12, 41]. These enrichment functions are identical to those defined in [12]. The corresponding generalized FE shape functions, $\hat{\phi}_{\alpha i}$, at a node \mathbf{x}_α , are polynomials of degree p given by

$$\hat{\phi}_{\alpha i}(\mathbf{x}) = \varphi_\alpha(\mathbf{x}) \hat{L}_{\alpha i}(\mathbf{x}) \quad i = 1, \dots, \hat{D}_L \quad (\text{no summation on } \alpha) \quad (6)$$

Local approximation for a discontinuous function Let \mathcal{I}_{c-f} denote a set with the indices of clouds ω_α that intersect the crack surface but not the crack front. Thus, the crack surface divides ω_α into two sub-domains, ω_α^+ and ω_α^- such that $\omega_\alpha = \omega_\alpha^+ \cup \omega_\alpha^-$. In this section, we define basis functions for local spaces $\chi_\alpha(\omega_\alpha)$, $\alpha \in \mathcal{I}_{c-f}$.

The elasticity solution \mathbf{u} over ω_α , $\alpha \in \mathcal{I}_{\text{c-f}}$, can be written as [48, 60]

$$\mathbf{u} = \hat{\mathbf{u}} + \tilde{\mathbf{u}} = \hat{\mathbf{u}} + \mathcal{H}\tilde{\mathbf{u}}$$

where $\hat{\mathbf{u}}$ and $\tilde{\mathbf{u}}$ are continuous functions and $\mathcal{H}(\mathbf{x})$ denotes a discontinuous function defined by

$$\mathcal{H}(\mathbf{x}) = \begin{cases} 1 & \text{if } \mathbf{x} \in \omega_\alpha^+ \\ 0 & \text{otherwise} \end{cases} \quad (7)$$

We assume that the crack faces, i.e. Γ_c^+ and Γ_c^- are not in contact. In the case of contact, the non-penetration condition can be enforced using, for example, a formulation based on distributed springs with very large stiffness in the direction normal to the surfaces [49].

A local approximation, $\mathbf{u}_\alpha^{hp}(\mathbf{x})$, of \mathbf{u} over ω_α , $\alpha \in \mathcal{I}_{\text{c-f}}$, can be written as

$$\mathbf{u}_\alpha^{hp}(\mathbf{x}) = \hat{\mathbf{u}}_\alpha^{hp}(\mathbf{x}) + \mathcal{H}\tilde{\mathbf{u}}_\alpha^{hp}(\mathbf{x}) = \sum_{i=1}^{\hat{D}_L} \hat{\mathbf{u}}_{\alpha i} \hat{L}_{\alpha i}(\mathbf{x}) + \sum_{i=1}^{\tilde{D}_L} \tilde{\mathbf{u}}_{\alpha i} \mathcal{H}\hat{L}_{\alpha i}(\mathbf{x})$$

where $\hat{\mathbf{u}}_\alpha^{hp}(\mathbf{x})$ and $\tilde{\mathbf{u}}_\alpha^{hp}(\mathbf{x})$ are local approximations of $\hat{\mathbf{u}}$ and $\tilde{\mathbf{u}}$, respectively, and $\hat{L}_{\alpha i}$ is a polynomial enrichment function of degree less than or equal to $p-1$ as previously defined.

The analysis of through-the-thickness cracks presented in [16] shows that the continuous and discontinuous components of the solution \mathbf{u} should be approximated using the same polynomial order. Thus, we take $\tilde{D}_L = \hat{D}_L$ in all computations presented in Section 5.

Based on the above, the generalized FE shape functions of degree less than or equal to p used at a node \mathbf{x}_α , $\alpha \in \mathcal{I}_{\text{c-f}}$, are given by

$$\Phi_\alpha^p = \{\hat{\phi}_{\alpha i}, \tilde{\phi}_{\alpha i}\}_{i=1}^{\hat{D}_L} \quad (8)$$

where $\tilde{\phi}_{\alpha i} = \mathcal{H}\hat{\phi}_{\alpha i}$ and $\hat{\phi}_{\alpha i}$ is defined in (6). The generalized FE shape functions for branched cracks presented in [16] reduce to Φ_α^p in the case of non-branching cracks. The enrichment functions $\mathcal{H}\hat{L}_{\alpha i}(\mathbf{x})$, $i = 1, \dots, \hat{D}_L$, are called high-order step functions [16].

Local approximation on a cloud that intersects the crack front Terms from the asymptotic expansion of the elasticity solution near crack fronts are good choices for enrichment functions in clouds that intersect the crack front. Expansions for three dimensional problems are discussed in, for example, [26, 39]. The intersection of a crack surface with the boundary of the domain creates complex stress distributions, which make the asymptotic expansions in these regions quite complex and in general, not practical for engineering applications. Currently, two dimensional expansions of the elasticity solution are used as enrichment functions for three-dimensional cracks in finite size domains [12, 15, 38, 53]. As a consequence, a sufficiently fine mesh must be used around the crack front to achieve acceptable accuracy.

Let $\mathcal{I}_{\text{front}}$ denote a set with the indices of clouds ω_α that intersect the crack front. In this paper, a local approximation, $\tilde{\mathbf{u}}_\alpha^{hp}(\mathbf{x})$, of \mathbf{u} over ω_α , $\alpha \in \mathcal{I}_{\text{front}}$, is defined as

$$\tilde{\mathbf{u}}_\alpha^{hp} = \sum_{i=1}^2 \begin{bmatrix} \tilde{\mathbf{u}}_{\alpha i}^\xi \tilde{L}_{\alpha i}^\xi(r, \theta) \\ \tilde{\mathbf{u}}_{\alpha i}^\eta \tilde{L}_{\alpha i}^\eta(r, \theta) \\ \tilde{\mathbf{u}}_{\alpha i}^\zeta \tilde{L}_{\alpha i}^\zeta(r, \theta) \end{bmatrix} \quad (9)$$

where ξ , η and ζ are directions in a Cartesian coordinate system and θ is a polar coordinate, as illustrated in Figure 4, $\check{u}_{\alpha i}^\xi$, $\check{u}_{\alpha i}^\eta$ and $\check{u}_{\alpha i}^\zeta$ are degrees of freedom in the ξ -, η - and ζ - directions, respectively. Here, the degrees of freedom are scalar quantities, in contrast with those used before. The enrichment functions are given by [12, 15, 40, 42]

$$\begin{aligned}
\check{L}_{\alpha 1}^\xi(r, \theta) &= \sqrt{r} \left[\left(\kappa - \frac{1}{2} \right) \cos \frac{\theta}{2} - \frac{1}{2} \cos \frac{3\theta}{2} \right] \\
\check{L}_{\alpha 1}^\eta(r, \theta) &= \sqrt{r} \left[\left(\kappa + \frac{1}{2} \right) \sin \frac{\theta}{2} - \frac{1}{2} \sin \frac{3\theta}{2} \right] \\
\check{L}_{\alpha 1}^\zeta(r, \theta) &= \sqrt{r} \sin \frac{\theta}{2} \\
\check{L}_{\alpha 2}^\xi(r, \theta) &= \sqrt{r} \left[\left(\kappa + \frac{3}{2} \right) \sin \frac{\theta}{2} + \frac{1}{2} \sin \frac{3\theta}{2} \right] \\
\check{L}_{\alpha 2}^\eta(r, \theta) &= \sqrt{r} \left[\left(\kappa - \frac{3}{2} \right) \cos \frac{\theta}{2} + \frac{1}{2} \cos \frac{3\theta}{2} \right] \\
\check{L}_{\alpha 2}^\zeta(r, \theta) &= \sqrt{r} \sin \frac{3\theta}{2}
\end{aligned} \tag{10}$$

where the material constant $\kappa = 3 - 4\nu$ and ν is Poisson's ratio. This assumes plane strain conditions, which is in general a good approximation far from crack front vertices.

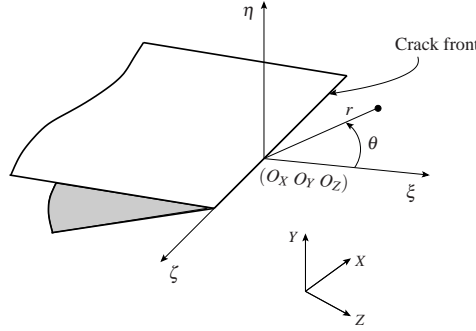


Figure 4: Coordinate systems associated with a crack front in 3-D space.

We can observe that the basis functions are given by the first term of the mode *I*, *II*, and the first and second terms of the mode *III* components of the asymptotic expansion around a straight crack front, far from the vertices and traction-free flat crack surface [55]. They can approximate the singularity of the exact solution along the crack front and the discontinuity of the displacement field. They also allow crack fronts arbitrarily located in a cloud ω_α . Thus, a crack front does not have to be located on element faces as in [1, 21, 22].

Generalized FEM shape functions built with the enrichment functions (10) must be integrated with care. In the numerical examples presented in this paper, this is achieved by using strongly graded meshes at the crack front and an appropriate number of integration points. The number of integration points depends on the level of accuracy aimed at for a particular problem. A detailed study of numerical integration and computational performance of these functions is presented in a forthcoming paper.

Different enrichment functions are used in (9) for each component of the displacement vector. This

leads to a total of six additional degrees of freedom at a node $\alpha \in \mathcal{I}_{\text{front}}$. More degrees of freedom would be required if the same enrichment functions are used for all components of the displacement vector. The enrichment functions used in, e.g., [9, 38, 52, 53], lead, in 3-D, to twelve enrichment functions for nodes in the set $\mathcal{I}_{\text{front}}$ since four enrichment functions are used for *each* component of the displacement vector. In the approach used in (9), only two enrichments are used to enrich each component of the displacement vector. The performance of these two choices of enrichment functions is analyzed in a forthcoming paper.

The basis functions (10) are defined in a coordinate system located along the crack front as illustrated in Figure 4. Thus, they must be transformed to the global Cartesian coordinate system (x, y, z) prior to their use in the definition of GFEM shape functions. Details can be found in, for example, [12, 15]. For future reference, let

$$\check{L}_{\alpha 1}^x, \check{L}_{\alpha 1}^y, \check{L}_{\alpha 1}^z, \check{L}_{\alpha 2}^x, \check{L}_{\alpha 2}^y, \check{L}_{\alpha 2}^z, \quad (11)$$

denote the result of such a transformation applied to the functions given in (10).

As discussed in Section 4, the crack front is represented as a piecewise linear object. Thus, the orientation of the local coordinate systems used to build the enrichment functions defined in (10) changes along the crack front and not all nodes $\alpha \in \mathcal{I}_{\text{front}}$ will use the same set of enrichment functions. In this paper, we apply the above enrichment functions only to clouds that intersect the crack front. This approach is denoted by *topological enrichment* in [6, 30]. An alternative is the so-called *geometrical enrichment* in which all nodes within a prescribed distance of the crack front are enriched, regardless of the mesh refinement around the crack front. The enrichment functions defined in (10) and those used in [6, 30] assume that the crack surface is planar. Thus, the geometrical enrichment is only suitable when the crack surface is planar in the (*not* necessarily small) sub-domain affected by the enrichment functions. Here, our goal is to model crack surfaces that may be arbitrarily curved and thus we employ topological rather than geometrical enrichment since the former assumes planar crack surfaces only in the clouds that intersect the crack front and the size of these clouds is small.

Examples Below we list a few examples of shape functions for tetrahedral elements using the definitions given above. Lets consider the elements shown in Figure 5. In the figure, yellow nodes belong to the set $\mathcal{I}_{\text{c-f}}$ while green nodes belong to the set $\mathcal{I}_{\text{front}}$.

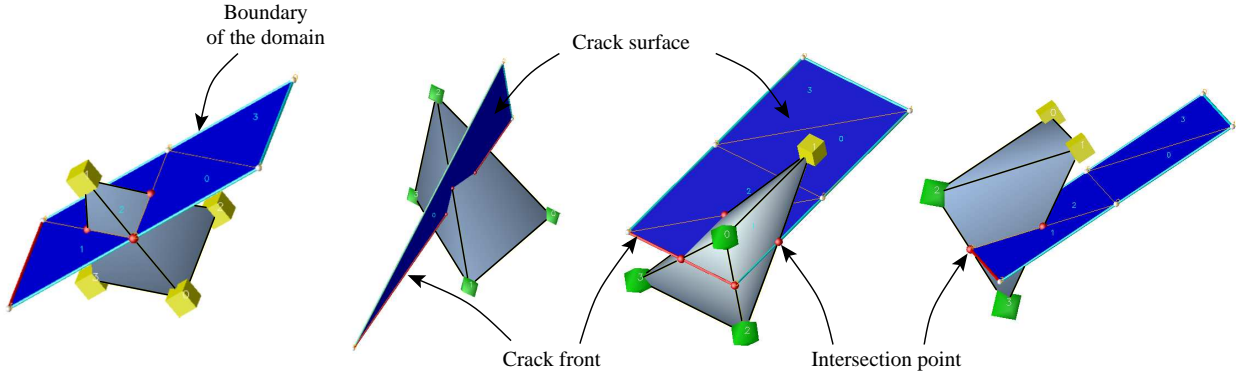


Figure 5: Examples of elements cut by a crack surface. Nodes with yellow glyphs belong to the set $\mathcal{I}_{\text{c-f}}$ while green nodes belong to the set $\mathcal{I}_{\text{front}}$. The crack front is represented by the red edge of the crack surface. Red glyphs represent intersections of element edges with the crack surface.

- *Linear Approximation:* In this case, the local approximations $\hat{\mathbf{u}}_{\alpha}^{hp}(\mathbf{x})$ and $\tilde{\mathbf{u}}_{\alpha}^{hp}(\mathbf{x})$ are constant over

ω_α and thus $\{\hat{L}_{\alpha i}\}_{i=1}^{\hat{D}_L=1} = \{1\}$. The shape functions at a yellow node \mathbf{x}_α are given by

$$\varphi_\alpha \times \{1, \mathcal{H}\} \quad (12)$$

These are the same shape functions used in, for example, [1, 9, 21, 22, 38, 52, 53, 60].

At a green node \mathbf{x}_α , the shape functions for the x -, y - and z - components of the displacement vector are given by

$$\varphi_\alpha \times \{1, \check{L}_{\alpha 1}^x, \check{L}_{\alpha 2}^x\}, \quad \varphi_\alpha \times \{1, \check{L}_{\alpha 1}^y, \check{L}_{\alpha 2}^y\}, \quad \text{and} \quad \varphi_\alpha \times \{1, \check{L}_{\alpha 1}^z, \check{L}_{\alpha 2}^z\}, \quad (13)$$

respectively. The enrichment functions used above are defined in (11).

- *Quadratic Approximation:* The local approximations $\hat{\mathbf{u}}_\alpha^{hp}(\mathbf{x})$ and $\tilde{\mathbf{u}}_\alpha^{hp}(\mathbf{x})$ are constant or linear over a cloud ω_α associated with node $\mathbf{x}_\alpha = (x_\alpha, y_\alpha, z_\alpha)$ and thus $\{\hat{L}_{\alpha i}\}_{i=1}^{\hat{D}_L=4} = \left\{1, \frac{(x-x_\alpha)}{h_\alpha}, \frac{(y-y_\alpha)}{h_\alpha}, \frac{(z-z_\alpha)}{h_\alpha}\right\}$. The shape functions at a yellow node \mathbf{x}_α are given by

$$\varphi_\alpha \times \left\{1, \frac{(x-x_\alpha)}{h_\alpha}, \frac{(y-y_\alpha)}{h_\alpha}, \frac{(z-z_\alpha)}{h_\alpha}, \mathcal{H}, \mathcal{H} \frac{(x-x_\alpha)}{h_\alpha}, \mathcal{H} \frac{(y-y_\alpha)}{h_\alpha}, \mathcal{H} \frac{(z-z_\alpha)}{h_\alpha}\right\}$$

These shape functions are defined in (8).

At a green node \mathbf{x}_α , the shape functions for the x -, y - and z - components of the displacement vector are given by

$$\begin{aligned} \varphi_\alpha \times \left\{1, \check{L}_{\alpha 1}^x, \check{L}_{\alpha 2}^x, \frac{(x-x_\alpha)}{h_\alpha}, \frac{(y-y_\alpha)}{h_\alpha}, \frac{(z-z_\alpha)}{h_\alpha}\right\}, \\ \varphi_\alpha \times \left\{1, \check{L}_{\alpha 1}^y, \check{L}_{\alpha 2}^y, \frac{(x-x_\alpha)}{h_\alpha}, \frac{(y-y_\alpha)}{h_\alpha}, \frac{(z-z_\alpha)}{h_\alpha}\right\}, \\ \varphi_\alpha \times \left\{1, \check{L}_{\alpha 1}^z, \check{L}_{\alpha 2}^z, \frac{(x-x_\alpha)}{h_\alpha}, \frac{(y-y_\alpha)}{h_\alpha}, \frac{(z-z_\alpha)}{h_\alpha}\right\}, \end{aligned}$$

respectively. Higher order shape functions for green nodes are defined analogously.

The numerical examples presented in Section 5 show that the generalized FEM shape functions presented above, combined with strongly graded meshes at the crack front, are able to deliver high convergence rates for stress intensity factors.

4 Crack Surface Representation and Integration of Weak Form

Section 4.1 presents a procedure to represent three-dimensional crack surfaces in a generalized finite element framework. We restrict the discussion to the case of non-branching crack surfaces but the procedure is also amenable to this case (Cf. [16]). The numerical integration of the weak form over elements cut by the crack surface is discussed in Section 4.2. Numerical examples demonstrating the robustness and accuracy of the proposed approach are also presented.

4.1 Crack Surface Representation

Several methods capable of representing a crack surface can be used with partition of unity methods like the GFEM. The choice of a particular method is mostly based on implementation considerations. In the approach proposed here, a three-dimensional crack surface is represented by an explicit triangulation of the surface. An example is depicted in Figure 6. The triangulation is completely independent of the underlying GFEM discretization. Thus, refinement of the volume GFEM mesh or a background mesh [9, 45, 52] are not needed in order to improve the representation of the crack surface, as is the case with implicit representations based on, for example, level set methods.

Additional features of the proposed crack surface representation include the following

- It provides support for the implementation of accurate, robust and computationally efficient numerical integration of the weak form over elements cut by the crack surface. This is not a trivial task since the integrand of the weak form is discontinuous, and possibly singular, over elements cut by the crack surface;
- The geometry of the crack surface is controlled only by the governing physics of the problem. Physically-consistent crack surface representations may be especially important in problems with loaded crack surfaces, or those involving cohesive fracture models [5, 20, 27];
- Adaptive control through refinement/unrefinement of the crack surface triangulation for accurate geometric representation.

In the examples presented in this paper, crack surfaces are represented using flat triangles with straight edges. Hereafter, we refer to these entities as *facets*. The facets do not need to define a valid finite element mesh as they are used for geometrical representation purposes only. Each facet has an orientation and thus we can identify if a given point in the 3-D domain is above, below or on the surface. The crack front is represented by straight line segments connecting the vertices of facet edges along the crack front. Thus, curved crack fronts are approximated by these straight line segments. The fidelity of this approximation can be controlled by simply using a finer triangulation of the crack surface. This process is independent of the GFEM mesh and does not change the problem size. Crack front segments are marked in red in the crack surfaces shown in Figures 5 and 6. Blue segments in the figures indicate segments that are on the boundary of the solution domain and thus can not propagate. Similar representation of crack surfaces can be found in, for example, [1, 15, 21, 22, 29].

4.2 Numerical Integration of Weak Form

Generalized FEM shape functions defined using enrichment functions (7) or (10) are discontinuous across the crack surface which, in turn, may be located inside a finite element as illustrated in Figure 5. Thus, special care must be taken when integrating the weak form over these elements. A common approach used to deal with this problem is to subdivide each computational finite element into integration sub-elements with faces fitting the crack surface and use standard quadrature rules over each sub-element [24, 37, 38, 48, 53, 54, 60]. These sub-elements, denoted hereafter as integration elements, are used solely for the numerical integration over their parent computational elements, and thus they do not introduce any additional degrees of freedom in the problem.

In the crack surface representation proposed above, we allow non-planar, non-smooth crack surfaces inside an element—the crack surface is not assumed to be planar inside an element. Therefore, the algorithm used to generate integration sub-elements must be able to handle this level of generality. Below, we describe an algorithm based on a Delaunay tetrahedralization [10] of elements cut by a crack surface. We assume

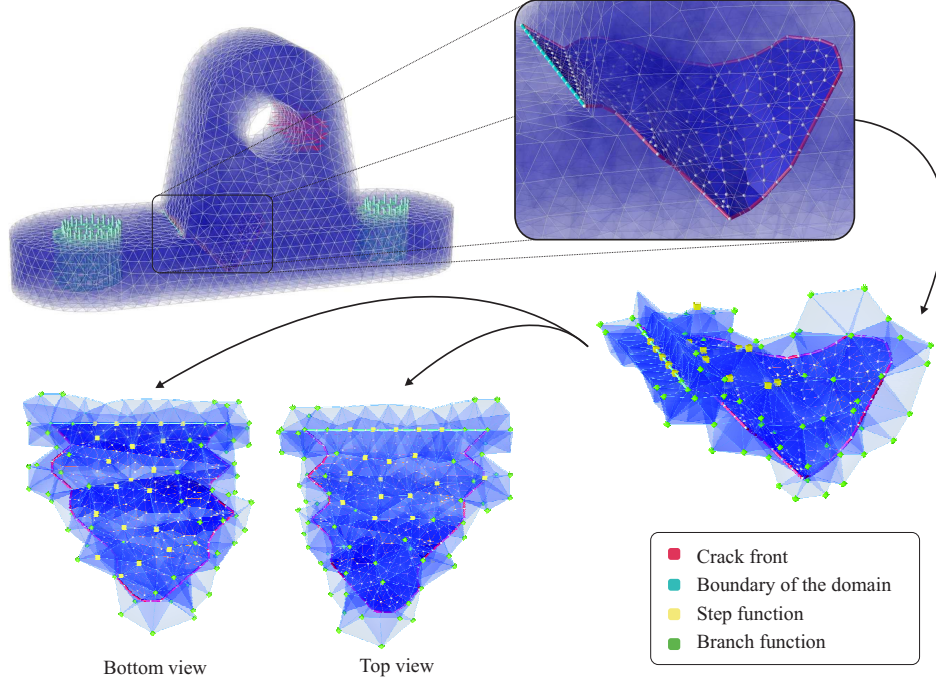


Figure 6: Example of arbitrary crack surface representation and selection of nodal enrichment in an unstructured three-dimensional mesh.

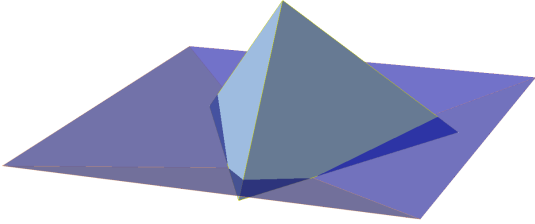
that the volume mesh is composed of tetrahedral elements. Modifications to handle other types of elements are not difficult, as long as they have planar faces. A hexahedral element, for example, can be divided into integration tetrahedral sub-elements before applying the algorithm described below. Alternatively, a Delaunay tetrahedralization similar to the one proposed below, could be applied directly to hexahedral elements with planar faces.

Given a crack surface and a tetrahedral (computational) element that intersects the surface (Figure 7(a)), the following steps are performed:

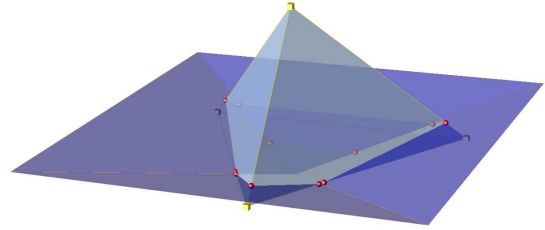
1. Compute the intersection of crack surface facets with faces of the computational finite element (Figure 7(b)).
2. Compute a Delaunay tetrahedralization [10] for the convex hull formed by the nodes of the computational element and the intersection points (Figure 7(c)). This step creates integration elements at both sides of the discontinuity.
3. Compute the orientation of the integration sub-elements with respect to the surface, i.e., define the position of the sub-elements with respect to the discontinuity (Figure 7(d)). This orientation is used in the computation of the step function defined in (7).

The integration over a computational element is given by the sum of the integrations over its sub-elements. Standard quadrature rules for tetrahedral elements are used at integration sub-elements. In the examples presented in this paper, we use the Keast quadrature rules introduced in [28].

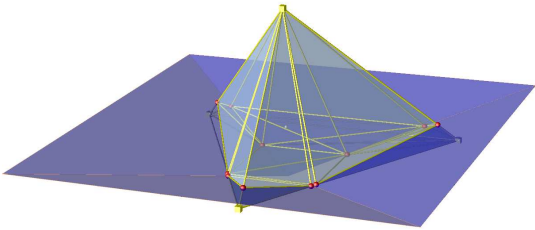
It is worth mentioning that the sub-elements do not need to define a valid finite element mesh since they are used for integration only. Thus, they can be generated on an element-by-element basis without



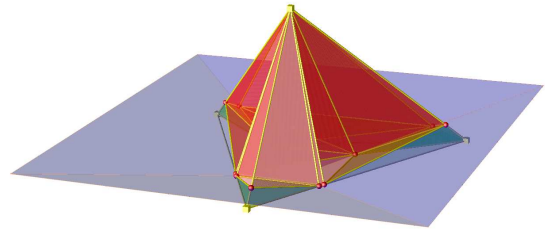
(a) A tetrahedral element intersected by a non-planar crack surface.



(b) Step 1: Intersection of crack surface facets with faces of the computational element.



(c) Step 2: Delaunay tetrahedralization.



(d) Step 3: Computation of orientation of integration sub-elements.

Figure 7: Construction of integration sub-elements of a tetrahedral element intersected by a non-planar crack surface.

enforcing continuity between integration elements that belong to neighboring computational elements. In addition, the integration of the weak form or the GFEM solution accuracy is not affected by the aspect-ratio of the sub-elements since they are not used to define the shape functions. This last point is numerically illustrated below. Under these relaxed conditions for the generation of integration sub-elements, Delaunay tetrahedralization is a very robust and computationally efficient algorithm [10].

The above algorithm is also used to create integration sub-elements for elements partially cut by a crack surface. In this case, the algorithm creates sub-elements with edges or vertices along the crack front, as illustrated in Figure 8. This feature is especially important when integrating enrichment functions that are singular in the radial direction of the crack front, like those defined in (10).

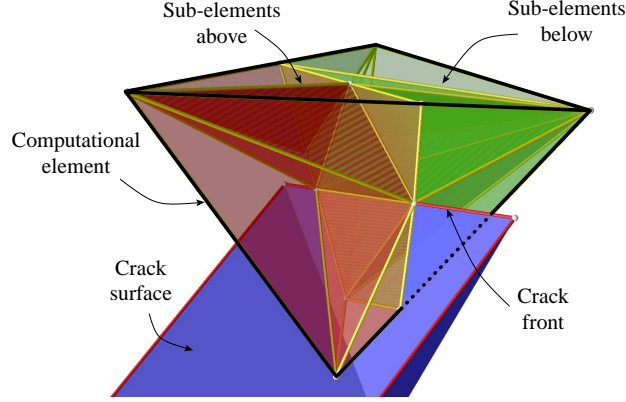


Figure 8: Integration sub-elements for a computational element partially cut by a crack surface. The computational element is represented by solid and dotted black lines. Sub-elements above and below the crack surface (or its extension) are represented in red and green colors, respectively. Edges of the sub-elements fit the crack front.

A high order or a special quadrature rule must be used to integrate non-polynomial enrichment functions like those defined in (10). In the examples presented in Section 5, we use 45 integration points over each integration sub-element of computational elements enriched with these functions. Fewer points may be used depending on the target error level for extracted stress intensity factors. In Section 5, we present several convergence studies and this high order quadrature rule was selected in order to guarantee that results and conclusions are not affected by numerical integration errors. Detailed discussion and analysis of the numerical integration of branch functions like those defined in (10) are presented in a forthcoming paper.

4.2.1 Numerical Experiments

The accuracy of the numerical integration over elements fully cut by non-planar crack surfaces is investigated in this section. The integration of the stiffness matrix is performed with the aid of the integration sub-elements generated by the algorithm described above. The examples demonstrate that the accuracy of the numerical integration is not affected by the large aspect ratios of the sub-elements.

Curved crack surface Figure 9(a) shows a computational element fully cut by a non-planar crack surface and its integration sub-elements. We can observe that most sub-elements have a large aspect ratio. The nodes of the computational element are enriched with continuous polynomial functions only (those defined in (5)). Thus, exact numerical integration can be performed using a Keast quadrature rule and the compu-

tational element. Of course, the discontinuity along the crack surface can not be represented by this choice of shape functions. *The crack surface was used here solely to trigger the creation of integration elements.* Table 1 lists the Frobenius norm of the element stiffness matrix computed with the computational element and with its integration sub-elements for various polynomial orders. The relative difference between the two norms is also presented. The same quadrature rule is used in the computational element and in each integration sub-element. The Frobenius norm of a square matrix \mathbf{A} of dimension n is defined as [59]

$$\|\mathbf{A}\|_F = \left(\sum_{i=1}^n \sum_{j=1}^n |a_{ij}|^2 \right)^{\frac{1}{2}}$$

From the table, we can observe that the integration sub-elements can integrate the stiffness matrix with the same accuracy as the parent computational element, in spite of their large aspect ratios.

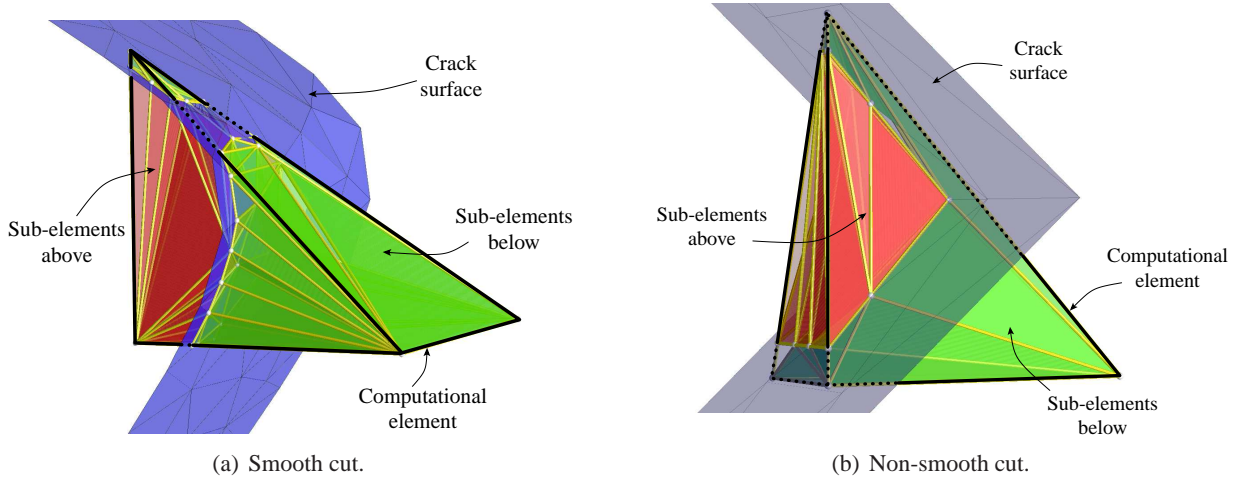


Figure 9: Computational elements with non-planar cuts and their integration sub-elements. The computational element is represented by solid and dotted black lines. The orientation of the sub-elements with respect to the crack surface is represented by their colors. Sub-elements above and below the crack surface are represented in red and green colors, respectively.

Table 1: Frobenius norm of the stiffness matrix of the computational element shown in Figure 9(a) computed with the computational element ($\|\mathbf{k}^e_{comp. elem.}\|_F$) and with integration sub-elements ($\|\mathbf{k}^e_{int. elem.}\|_F$).

p-order	$\ \mathbf{k}^e_{comp. elem.}\ _F$	$\ \mathbf{k}^e_{int. elem.}\ _F$	$\frac{ \ \mathbf{k}^e_{comp. elem.}\ _F - \ \mathbf{k}^e_{int. elem.}\ _F }{\ \mathbf{k}^e_{comp. elem.}\ _F}$
1	1.0972591518348518	1.097259151834852	2.02e-16
2	1.2517652266704329	1.2517652266704324	3.55e-16
3	1.278954417398664	1.2789544173986642	1.74e-16
4	1.2844325919324189	1.2844325919324218	2.25e-15
5	1.2856390512282414	1.2856390512282432	1.38e-15

Crack with non-smooth surface The above numerical experiment was repeated for the case of a non-smooth crack surface. Figure 9(b) illustrates this case. The results are presented in Table 2. Like in the previous case, the sub-elements are able to numerically integrate the stiffness matrix very accurately using standard Keast quadrature.

Table 2: Frobenius norm of the stiffness matrix of the computational element shown in Figure 9(b).

p-order	$\ \mathbf{k}^e_{comp.elem.}\ _F$	$\ \mathbf{k}^e_{int.elem.}\ _F$	$ \ \mathbf{k}^e_{comp.elem.}\ _F - \ \mathbf{k}^e_{int.elem.}\ _F $
			$\ \mathbf{k}^e_{comp.elem.}\ _F$
1	1.0972591518348518	1.0972591518348522	4.05e-16
2	1.2517652266704329	1.2517652266704333	3.55e-16
3	1.278954417398664	1.2789544173986651	8.68e-16
4	1.2844325919324189	1.2844325919324193	3.46e-16
5	1.2856390512282414	1.2856390512282416	1.73e-16

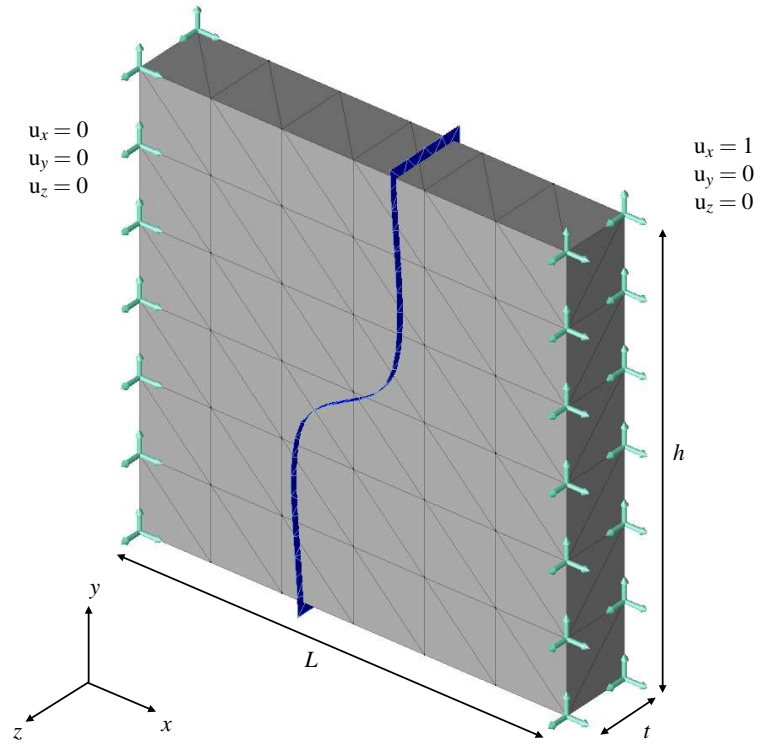
Separation test The main objective of this example is to show that the aspect ratios of the integration sub-elements do not affect the solution of the problem in a global sense. The boundary value problem analyzed in this section is depicted in Figure 10(a). Displacement boundary conditions are prescribed on element faces that are orthogonal to the x -axis. In this example, the crack surface cuts the entire domain separating it into two parts. Since the crack front does not intersect any element in the volume mesh, the discontinuous solution can be discretized using only the high order step functions $\tilde{\phi}_{\alpha i}$ defined in Section 3.2. The material and geometry parameters are taken as $E = 2.0 \times 10^5$, $\nu = 0.30$, and $L = h = 6.0$, $t = 1.0$, respectively. Of course, these parameters do not play any role in the simulation since the resulting strain energy of the system is zero.

The separation test is performed using smooth and non-smooth crack surfaces as illustrated in Figures 10(b) and 10(c), respectively. Table 3 lists the strain energy values for these two cases. One can observe that the aspect-ratio of the integration sub-elements does not affect the solution since the error in strain energy is of the order of machine precision.

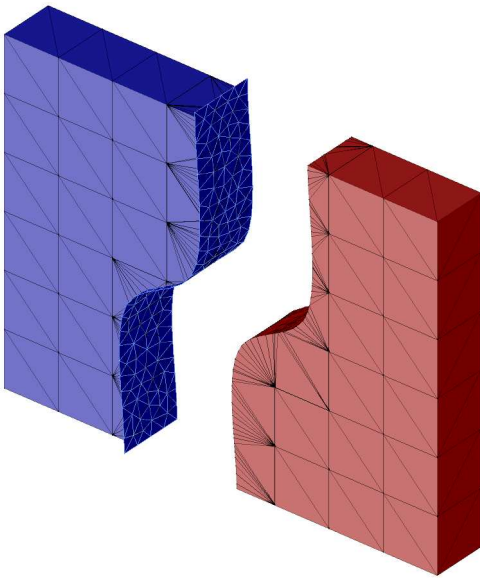
Table 3: Strain energy for the separation test with smooth and non-smooth interface.

p-order	U_{smooth}	$U_{non-smooth}$
1	5.6412993017109327e-28	1.62e-29
2	1.088053440658176e-24	5.56e-27
3	2.2944093170070629e-14	7.18e-24
4	6.1029505746932564e-15	1.23e-15
5	1.9831522943527249e-14	5.14e-15

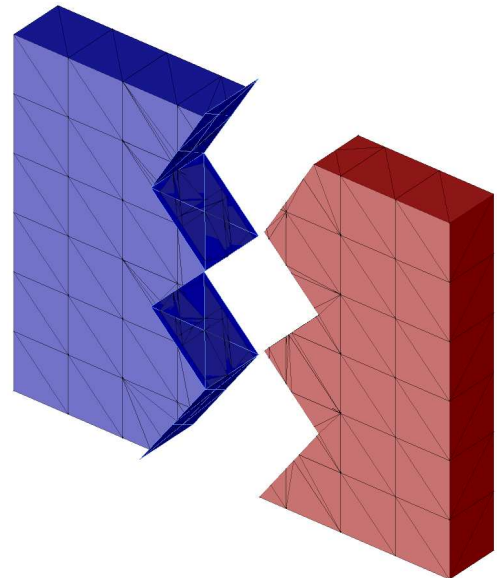
The results presented in this section, show that the proposed approach to integrate the weak form is robust, accurate and computationally efficient. It allows numerical integration over elements containing arbitrarily non-planar cuts. Also, this approach can handle coarse volume GFEM meshes cut by quite arbitrary crack surfaces.



(a) Separation test - Problem description.



(b) Smooth cut.



(c) Non-smooth cut.

Figure 10: Separation test for smooth and non-smooth discontinuities.

5 Numerical Examples

This section presents the numerical analyses of several three-dimensional fracture mechanics problems with increasing level of complexity. The complexity of the problems ranges from simple cracked bar to an industrial level problem with non-trivial geometry. All problems are solved using four-node tetrahedral volume meshes for domain discretization, triangular surface meshes for crack surface representation and hierarchical polynomial enrichment with localized mesh refinement at crack fronts. The aim of this section is to show the robustness and accuracy of the proposed approach when solving these problems.

In the examples presented in this section, the extraction of stress intensity factors (SIF) for planar and non-planar cracks is performed by applying the cut-off function method (CFM) and the contour integral method (CIM), respectively. These are superconvergent extraction techniques based on Betti's reciprocity law and, as such, deliver convergence rates for SIFs that are as fast as the convergence rate for strain energy [44, 55, 56]. This feature of the CFM and CIM is also verified in the numerical examples.

5.1 Edge Cracked Bar

In this section, we analyze an edge cracked bar problem. It consists of a rectangular bar with a through-the-thickness edge crack as illustrated in Figure 11. The model is subjected to a uniform tensile traction applied at both ends. Displacement boundary conditions are applied only to prevent rigid body motion. Li et al. [31] solved this problem using boundary element techniques which are known for delivering accurate solutions for fracture mechanics problems. In order to allow a comparison with their numerical solution for stress intensity factors, the geometric parameters are set as $h/t = 0.875$, $a/t = 0.5$ and $w/t = 1.5$. For the material properties, we set Poisson's ratio $\nu = 1/3$ and Young's modulus $E = 1.0$. This example is used to numerically verify the discretization approach presented in Section 3 and to set some parameters such as the element size at the crack front and the polynomial order of enrichment functions to be used in subsequent examples.

Since there is no closed form solution for this problem, we use *a posteriori* error estimates [55] to compute a reference value for the strain energy. In this example, the reference value is computed using the p -version of the GFEM presented in [12], i.e., hierarchical continuous polynomial enrichment functions and a mesh with double nodes to represent the discontinuity. The computed reference value for strain energy is, for $a = 1$,

$$U_{ref} = 1.37387247299454 \times 10^{-4}.$$

The stress intensity factors as well as the strain energy are used to verify the convergence rates of the present approach.

5.1.1 Convergence and computational cost analyses

In this section, we perform a p -convergence analysis using a mesh locally refined at the crack front and crack vertices (hereafter referred to as hp -GFEM). The resulting polynomial order of the approximation ranges from $p = 1$ to $p = 4$. The mesh is designed in such a way that the ratio of the element size to the characteristic length of the crack (L_e/a) is around 3.1×10^{-2} for those elements that intersect the crack front, 1.6×10^{-4} for those elements intersecting crack vertices, and 1.67 for the elements far from the crack front and crack vertices (Cf. Figure 12(a)). This mesh can be regarded as coarse when compared with those used with standard low order finite elements. The mesh used in this analysis and the displacement solution for $p = 4$ are illustrated in Figure 12(a). For comparison, we solve the same problem using quasi-uniform

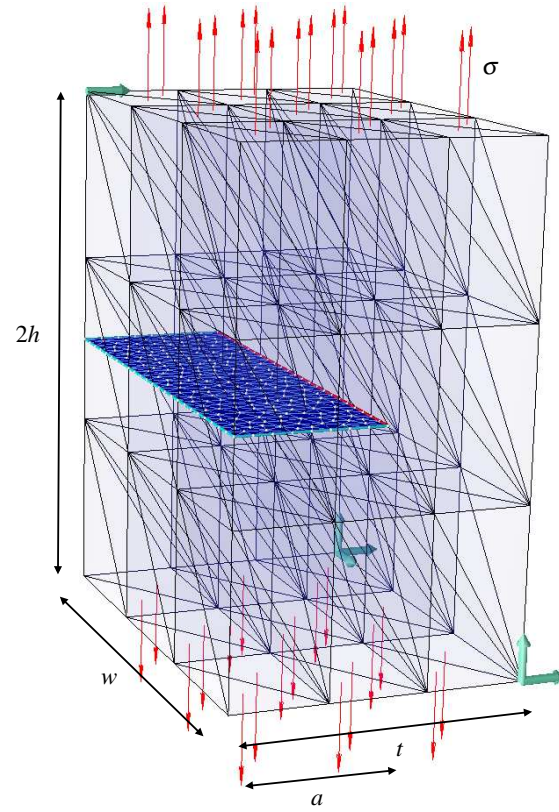


Figure 11: *Edge cracked bar: Initial coarse mesh with boundary conditions and crack surface representation.*

meshes and low-order shape functions defined in (12) and (13). Hereafter, this type of discretization is referred to as h -GFEM. One of the h -GFEM meshes used in the analysis and its respective solution are illustrated in Figure 12(b).

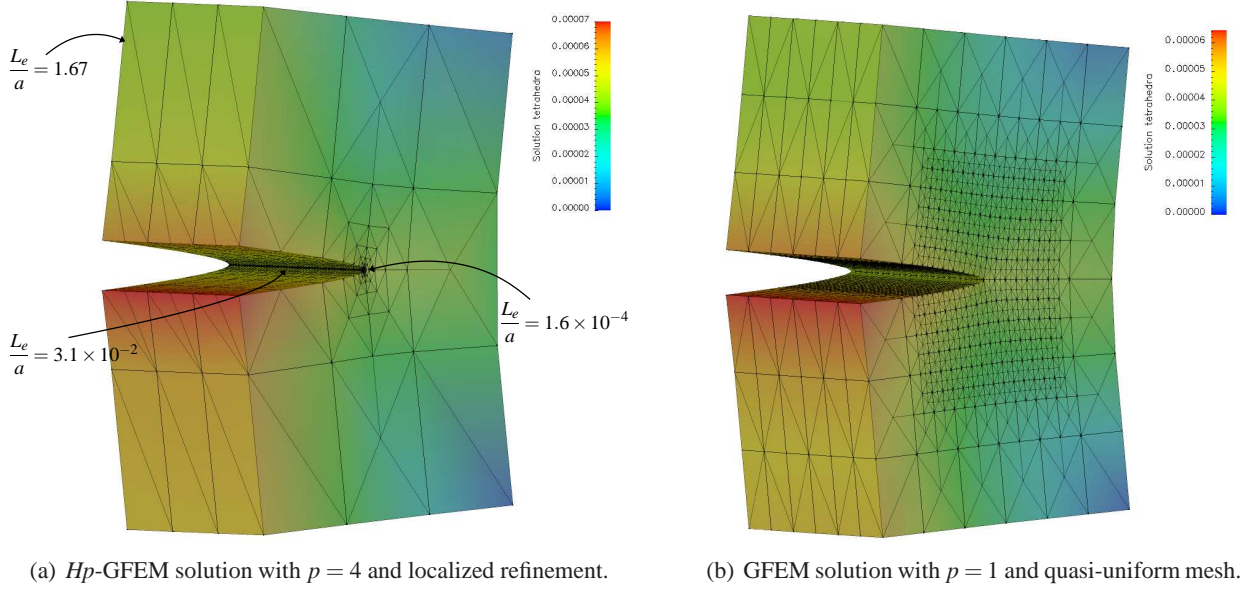


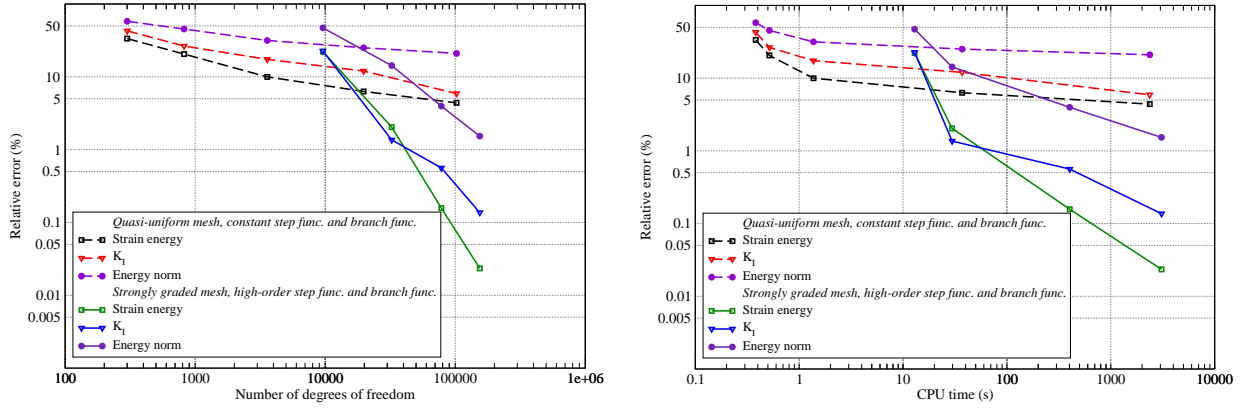
Figure 12: Mesh design and solution for hp -GFEM with localized refinement and GFEM with quasi-uniform mesh.

Figure 13(a) shows the variation of the error in energy norm, strain energy and the stress intensity factor (SIF) in the center of the crack front with respect to the number of degrees of freedom for both h - and hp -GFEM. One can observe that for relative errors smaller than about 7% in energy or SIF, the hp -GFEM is always more effective than the h -GFEM. In the case of relative error in energy norm, the threshold is even higher—about 30%. Moreover, hp -GFEM delivers exponential convergence while h -GFEM exhibits algebraic convergence. As expected, the extracted SIF shows a convergence behavior that is comparable to the convergence in strain energy in both h - and hp -GFEM. In this example, we can see that an approximation of order $p = 3$ is enough to deliver a relative error level around 1% for both strain energy and SIF.

In Figure 13(b), one can observe the variation of the relative error in energy norm, SIF and strain energy with respect to the CPU time spent to solve the problem using different meshes in h -GFEM and different polynomial orders in hp -GFEM. The CPU time consists of the time spent in assembling and solution of the system of equations. The linear dependence of the system was handled using the algorithm presented in [12]. For a given computational effort, the hp -GFEM with shape functions of p -order $p > 1$ provides more accurate results than h -GFEM. This is the same trend observed in Figure 13(a),

5.1.2 SIF extraction along crack front

A particular feature of the edge-cracked bar example is the variation of the mode I stress intensity factor along the crack front. It varies from a nearly plane strain SIF value at the middle of the crack front to asymptotically zero at the crack vertex. The stress intensity factor tends to zero when the crack front intersects the boundary of the domain because the singularity of the solution is less intense in that region [31, 46].



(a) Convergence analysis - relative error vs. number of degrees of freedom.

(b) Cost analysis - relative error vs. total CPU time.

Figure 13: Convergence and computational cost analyses.

Figure 14(a) shows the normalized SIF extracted along the crack front using the hp -GFEM solution for $p = 1, \dots, 4$. The normalized SIF is defined as

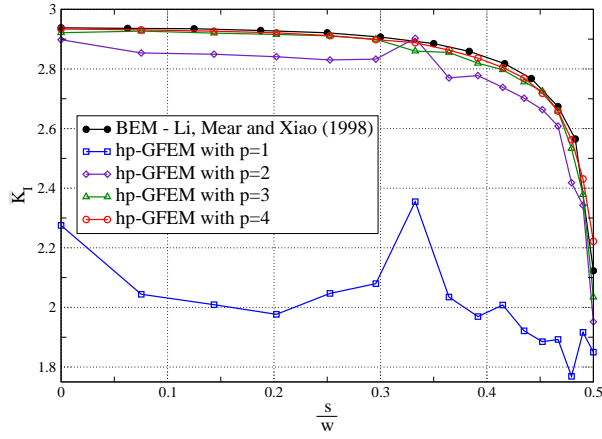
$$\bar{K}_I = \frac{K_I}{\sigma \sqrt{\pi a}}$$

where K_I is the stress intensity factor computed numerically. The results are plotted in parametric coordinates at the crack front in which $s/w = 0.0$ corresponds to the middle of the crack front and $s/w = 0.5$ corresponds to a crack vertex. We can observe that the hp -GFEM solution clearly converges to the BEM solution of Li and Mear [31], as the polynomial order of the approximation is increased. The hp -GFEM results along the crack front are also consistent with the convergence analysis presented above, namely, the results for $p = 3$ have already reached an acceptable level of accuracy for engineering purposes.

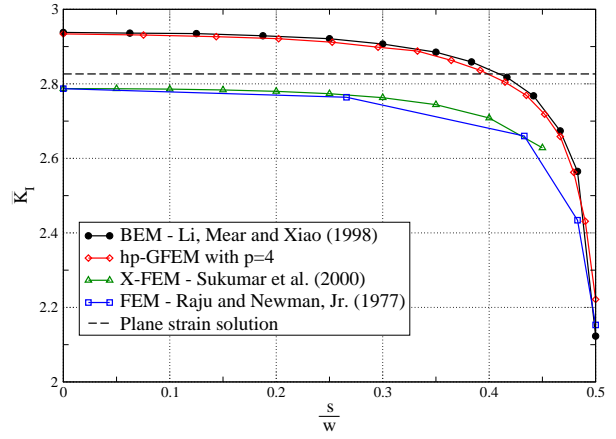
Many researchers have solved this problem using different techniques such as the standard finite element with quarter-point elements [46], the X-FEM with hexahedral elements [53], and the boundary element method [31]. Figure 14(b) shows a comparison among these solutions, a plane strain solution and the hp -GFEM solution for $p = 4$. One can observe that the hp -GFEM solution shows good agreement with the BEM solution and can capture very well the boundary layer behavior of K_I .

Nearly optimal distribution of degrees of freedom In the examples presented above, the hp -GFEM is applied using uniform polynomial enrichment over the entire domain. Of course, application of uniform enrichment in problems of industrial level of complexity is unacceptable because it leads to a high number of degrees of freedom. However, the hp -GFEM formulation is flexible enough to provide non-uniform polynomial approximations over a domain of analysis. One can build an approximation applying high order enrichment functions only where needed. According to [41, 55], an optimal hp discretization for fracture mechanics problems consists of h -refinement in geometrical progression towards the singularity and p -enrichment of increasing p -order away from the singularity.

Figure 15(b) shows a comparison of the results computed with hp -GFEM using uniform ($p = 3$) and non-uniform polynomial order. The same mesh (cf. Figure 12(a)) is used in both cases but in the later, the p -order decreases towards the singularity, as illustrated in Figure 15(a). The number of degrees of freedom



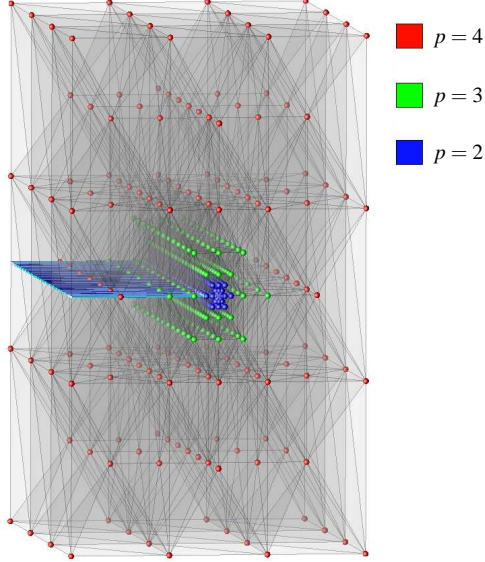
(a) SIF extraction using *hp*-GFEM with various p .



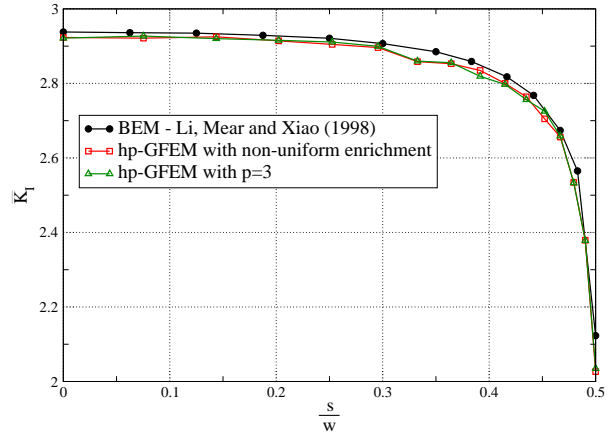
(b) Comparison with SIF values in the literature.

Figure 14: Extraction of SIF along the crack front for edge cracked bar example.

in the solution with uniform p -enrichment is 78,234 while in the non-uniform distribution is 45,774, which gives a problem size reduction of more than 40%. The CPU time spent in the simulation with uniform and non-uniform p -enrichment was around 402 seconds and 254 seconds, respectively, which gives a computational cost reduction of 37%. By using this approach, we can save many unnecessary degrees of freedom in the approximation while achieving an equivalent level of accuracy. Hence, this approach is more attractive when solving large scale problems. An example of non-uniform enrichment applied to a problem with industrial level of complexity is presented in Section 5.4.



(a) GFEM discretization with non-uniform p -enrichment. The color of the sphere at a node indicates the polynomial order used over the corresponding nodal support.



(b) SIF extraction along the crack front - uniform polynomial enrichment vs. nearly optimal distribution of dofs.

Figure 15: SIF extraction using *hp*-GFEM with uniform and non-uniform p -enrichment.

5.2 Planar Penny-Shaped Crack

In this section, we use the well-known penny shaped crack example to numerically verify the accuracy of the extracted stress intensity factors (SIF) along a curved crack front of a planar surface. Consider a crack of circular shape with radius a localized in the center of a cube with dimension $2L$ as illustrated in Figure 16. The specimen is subjected to an axial tensile loading of magnitude σ in y -direction. The numerical values for the dimensions of the model and the magnitude of the axial tensile loading are $\frac{L}{a} = 10$ and $\sigma = 1.0$, respectively.

Figure 16 illustrates the initial tetrahedral mesh, boundary conditions and crack surface representation used in the numerical model. This mesh is automatically h -refined along the crack front as illustrated in Figure 17. We can observe that the aspect ratio of the elements is preserved with mesh refinement since element faces do not have to fit the crack surface as in the classical FEM. The ratio of element size to characteristic length of the crack surface ranges from $\{L_e/a\}_{max} = 3.38 \times 10^{-2}$ to $\{L_e/a\}_{min} = 1.95 \times 10^{-2}$ at the crack front. In this example, we perform a p -convergence analysis using the mesh shown in Figure 17. The polynomial order of the enrichment varies from $p = 1$ to $p = 3$. The selection of GFEM shape functions assigned to nodes depends on the behavior of the solution in the support, ω_α , of the node, as discussed in Section 3.2.

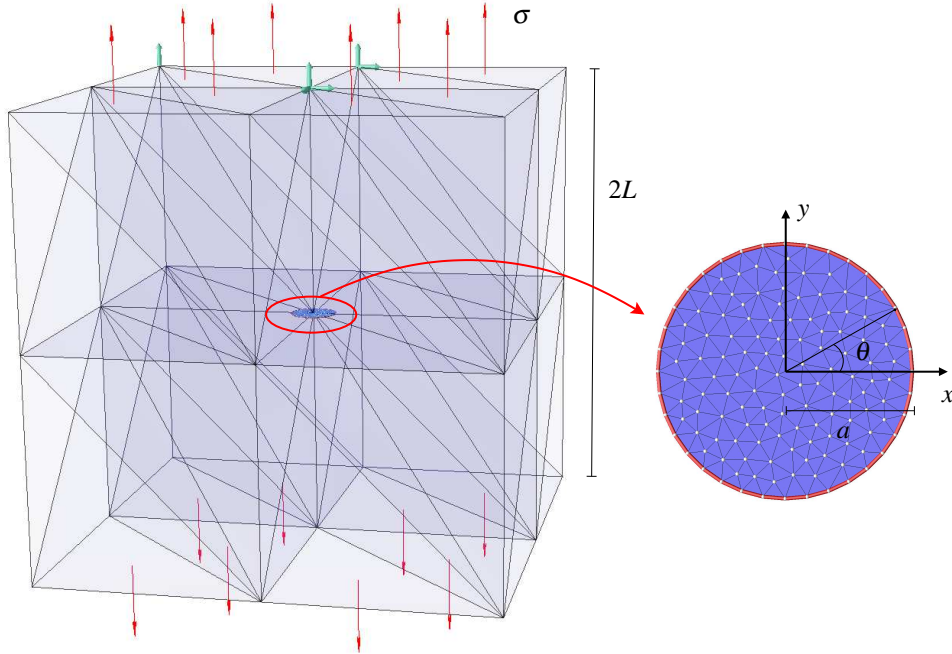


Figure 16: Penny shaped crack example: initial coarse mesh with boundary conditions and crack surface representation.

Figure 18 shows a plot with the normalized stress intensity factors along the crack front. The normalized SIF is given by [57]

$$\bar{K}_I = \frac{K_I}{K_I^\infty}$$

where K_I^∞ is the closed form solution of the penny shaped crack problem for an infinite domain, which is

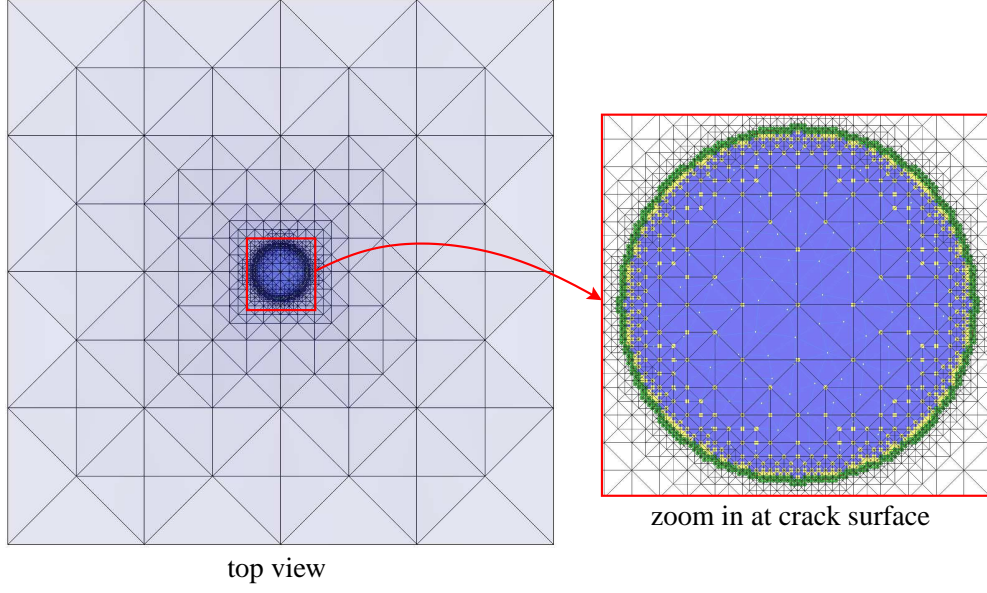


Figure 17: Tetrahedral mesh strongly graded at the crack front. The type of GFEM shape functions used at some nodes are also illustrated. Nodes with yellow glyphs have the GFEM shape functions $\tilde{\phi}_{\alpha i}$ defined in (8). In this case, the continuous and discontinuous shape functions are of the same polynomial order. Nodes with green glyphs have GFEM shape functions built with the functions defined in (11).

given by

$$K_I^\infty = 2\sigma\sqrt{\frac{a}{\pi}}.$$

This reference solution is commonly used to normalized solutions computed in finite domains. Normalized SIFs computed by Sukumar et al. [53] using the X-FEM [37] are also shown in the figure. In this case, the same domain/crack size ratio, $\frac{L}{a}$, and a structured mesh of eight-node hexahedral elements were used.

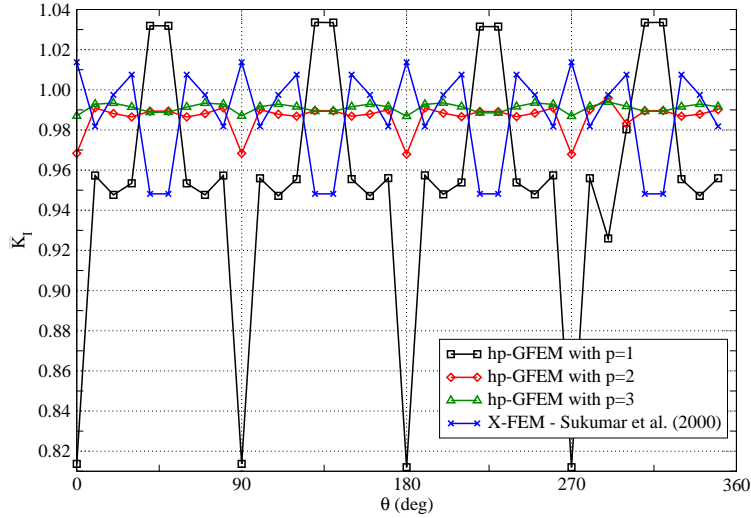


Figure 18: Stress intensity factor vs. position of the extraction at the crack front for various p order.

Table 4 lists the maximum, minimum, average and standard deviation of the relative error of the SIF extracted from hp -GFEM solutions with respect to the infinite domain solution. The results show good agreement with the analytical value for infinite domain. The average error for the solution enriched with $p = 3$ compared with the infinite domain solution is less than 1%. We can also see that the relative error values show fast convergence as the polynomial order of the approximation increases.

Table 4: Penny-shaped crack example: SIF relative error analysis for hp -GFEM for various p orders.

$er(\bar{K}_I)$	$p = 1$	$p = 2$	$p = 3$
Max	18.80	3.21	1.32
Min	1.97	0.41	0.60
Average	5.94	1.35	0.90
Std. Dev.	4.68	0.69	0.21

5.3 Lens-Shaped Crack

In this example, we consider a lens-shaped crack problem. This numerical example is more challenging than the problem presented in Section 5.2 because, in addition to the curved crack front, this crack surface is non-planar. Consider a lens-shaped crack of characteristic parameters R and α (cf. Figure 19) embedded in a cube of edge $2L$. The material parameters used in this example are $E = 68.9 \times 10^9$ and $\nu = 0.22$. The specimen is subjected to a hydrostatic tensile loading of magnitude σ . Again, we extract the stress intensity factors (SIF) along the crack front in order to numerically verify the proposed approach to solve crack problems. The CIM is used in this example to extract stress intensity factors. While the CIM is, in general, less accurate than the CFM, it also shows superconvergent behavior [44, 55, 56]. In addition, the implementation of the CIM is more straightforward than the CFM, especially in the case of non-planar crack surfaces.

Figure 19 depicts the initial coarse mesh, the boundary condition of the model and the representation of the crack surface. The geometry of the problem is defined such that the effect of the boundary of the domain in the extraction of the stress intensity factors is minimal. The numerical values for the characteristic parameters of the model and the magnitude of the hydrostatic tensile loading are $\frac{L}{R} = 5$, $\alpha = \frac{\pi}{4}$ and $\sigma = 1.0$, respectively. The results computed on this finite domain are compared with the analytical values for an infinite domain. If one considers the same crack geometry but embedded in an infinite domain, the analytical values of stress intensity factors for modes I and II are given by [23]

$$K_I^\infty = 0.877 \frac{2}{\pi} \sigma \sqrt{\pi a}, \quad K_{II}^\infty = 0.235 \frac{2}{\pi} \sigma \sqrt{\pi a} \quad (14)$$

where $a = R \cos(\alpha)$.

The discretization applied to this problems is the same as in the previous examples—strongly graded mesh at the crack front, crack front enrichment and high order step functions. The tetrahedral mesh is adapted with localized refinement along the crack front. The ratio of the size of the elements at the crack front to the characteristic length of the crack ($\frac{L_c}{a}$) ranges between 0.013 and 0.024. The polynomial order of the approximation used in this example is $p = 3$.

Figure 20 shows the normalized stress intensity factors for mode I and II . The normalized SIF is given

by

$$\bar{K}_i = \frac{K_i}{\frac{2}{\pi} \sigma \sqrt{\pi a}}$$

for a given mode i . If we compare the extracted quantities with the solution for an infinite domain, the SIFs for mode I and II converge to values around 6% larger and 8% smaller, respectively, than the reference values. These are less accurate results than in the previous examples even though comparable discretizations are used. We believe this is due to the extraction method used. The CIM uses derivatives of the numerical solution while the CFM uses only primary variables (displacements in the case of elasticity problems). Thus, as indicated above, SIFs extracted with the CIM are of lower accuracy than those extracted with the CFM. Nonetheless, we can observe that in Figure 20 the extracted SIFs are almost constant along the crack front, attesting the robustness of the extraction procedure and the accuracy of the solution. Figure 20 also shows SIFs computed with the finite element method on a finite cylinder and a domain integral method for extraction [23]. In this case, the radius and the height of the cylinder were 10 times the geometrical parameter R . An eight-node hexahedral mesh with $\frac{L_e}{a} \approx 0.0028$ was used around the crack front.

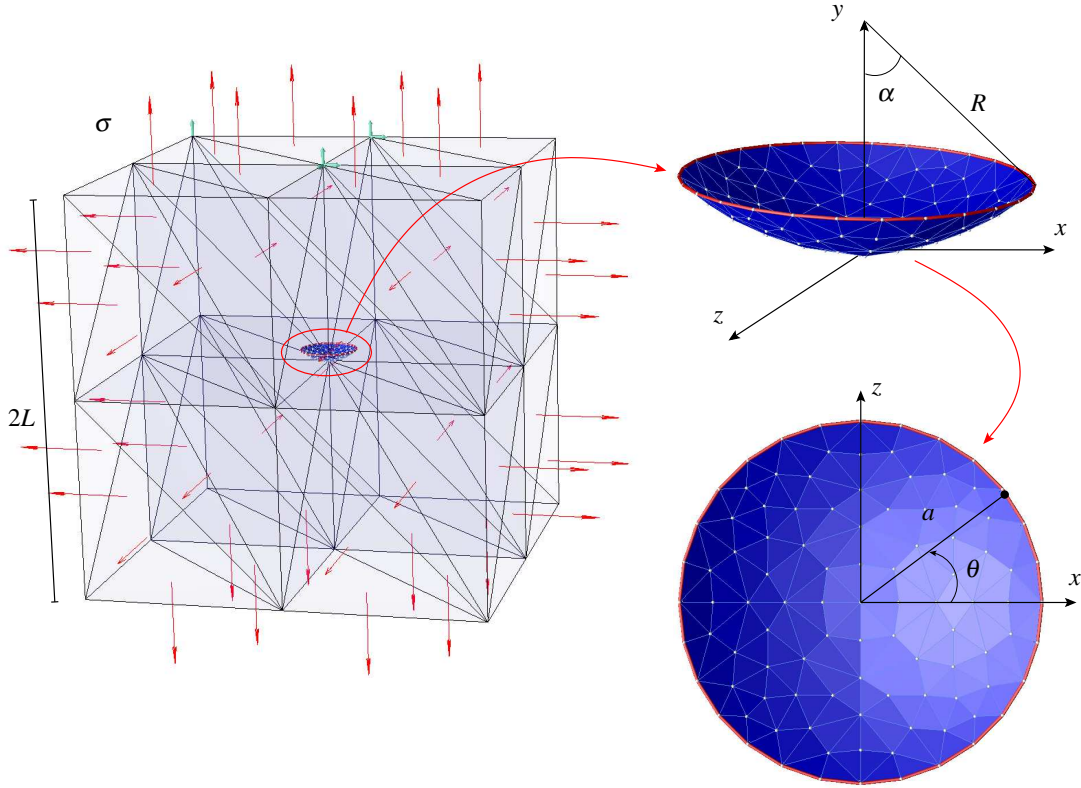


Figure 19: *Lens-shaped crack example: initial coarse mesh with boundary conditions and crack surface representation.*

5.4 Industrial example - a pump part

In this section, we solve a problem of industrial level of complexity. The example illustrated in this section consists of a pump part. The initial mesh, boundary conditions and crack surface representation are illus-

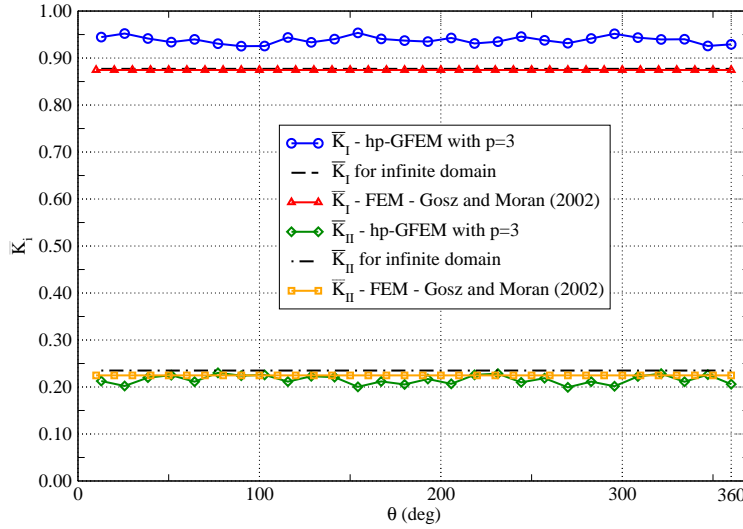


Figure 20: Normalized stress intensity factor for mode I and mode II along crack front.

trated in Figure 21. As in previous examples, the initial mesh does not model the crack surface. The crack surface is created later on using available geometric information of the model. The crack surface geometry is then discretized with triangles. The resulting triangulation is inserted in the model and mesh refinement as well as polynomial enrichment with respect to the crack front are automatically applied. This automation is easily applied in *hp*-GFEM since the mesh does not have to fit the crack surface representation and the non-uniform polynomial enrichment does not require transition elements. The resulting discretization around the crack surface is illustrated in Figure 22.

In this example, the crack surface has a circular front of radius $a = 0.22$. We take this radius as the characteristic length of the crack. The ratio of element size to characteristic crack length (L_e/a) is 2.10 for those elements far away from the crack surface. Around the crack front, L_e/a ranges from 0.023 to 0.16. The polynomial order of the approximation is $p = 2$ for the first layer of elements intersecting the crack front, $p = 3$ for the four subsequent layers, and $p = 2$ elsewhere. Figure 22 illustrates the *hp*-GFEM solution using *h*-refinement at the crack front and non-uniform enrichment. The material parameters for this example are $E = 2.0 \times 10^5$ and $\nu = 0.30$. This example illustrates the robustness and flexibility of the proposed approach where localized mesh refinement and non-uniform polynomial enrichment can be easily applied even in the case of non-trivial geometries.

To verify the results of the discretization described above, we solve this example using the same mesh and uniform polynomial enrichment of order $p = 4$. Table 5 lists the number of degrees of freedom and the strain energy using both discretization. We can see that the solution using non-uniform discretization requires around four times less degrees of freedom and has an error of 4.8% in strain energy. The stress intensity factors extracted along the crack front using non-uniform polynomial enrichment are compared with the reference solution. The extracted K_I and K_{II} are plotted in Figures 23(a) and 23(b). The results for SIF extraction using non-uniform enrichment also show good agreement with respect to the reference solution. The relative error of the maximum SIF computed with non-uniform enrichment with respect to the maximum SIF computed with uniform enrichment is 2.9% and 1% for K_I and K_{II} , respectively. These results show that one only needs to use high-order approximations locally in order to achieve an engineering acceptable level of accuracy in SIF.

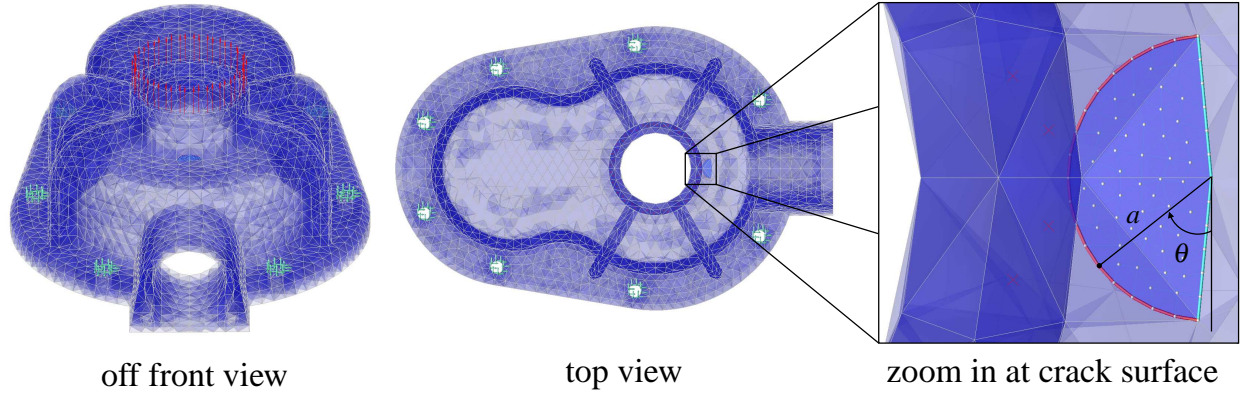


Figure 21: Model description and crack surface representation. Three-dimensional mesh courtesy of ABAQUS, Inc.

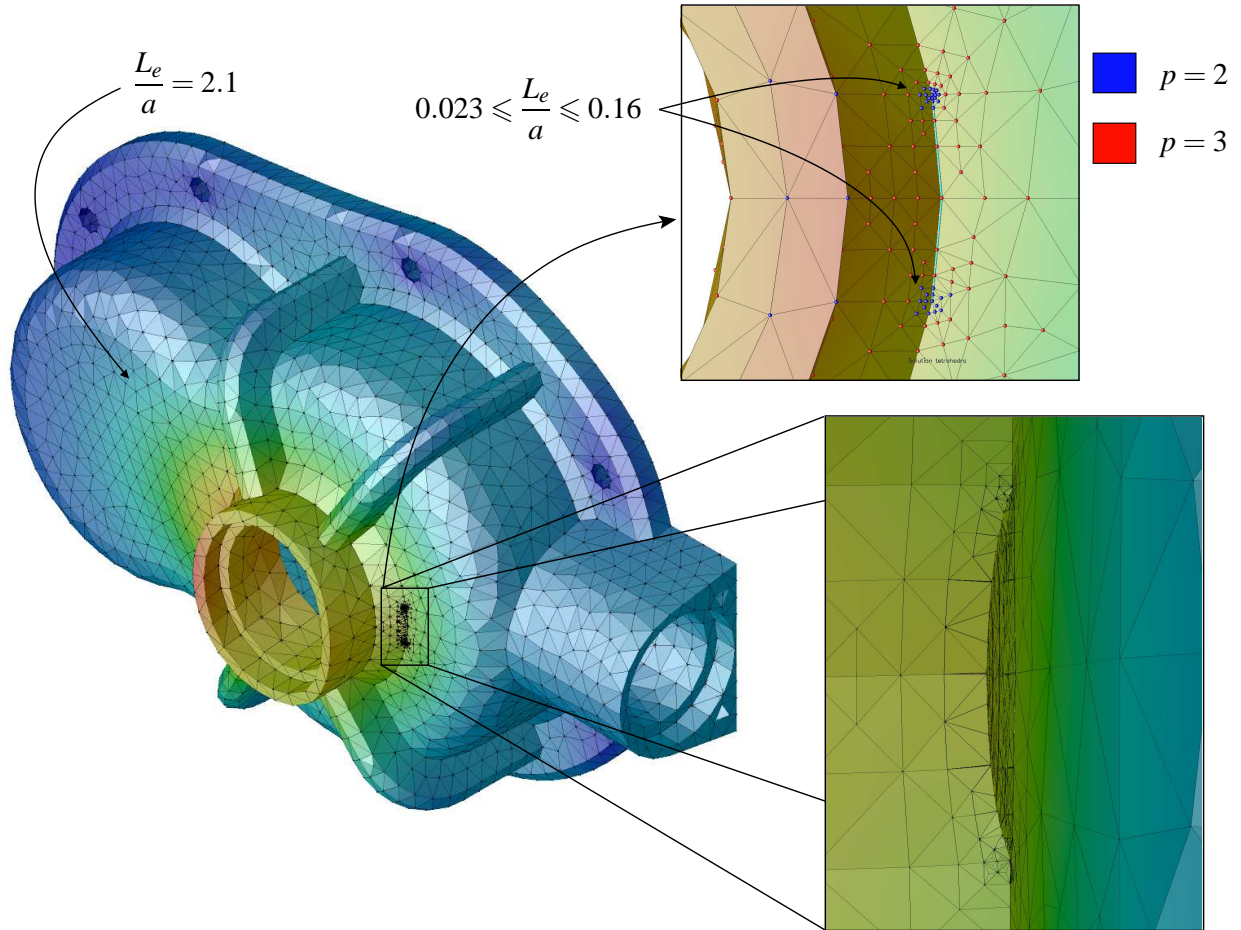
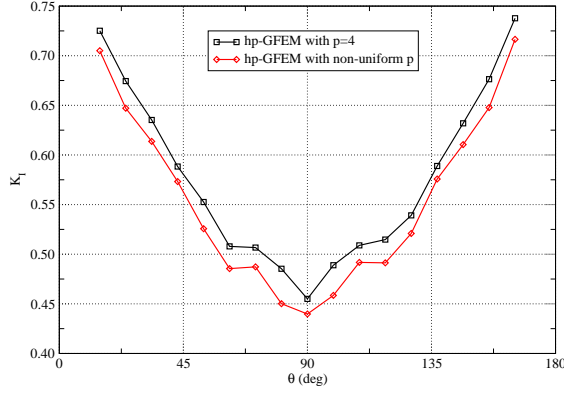


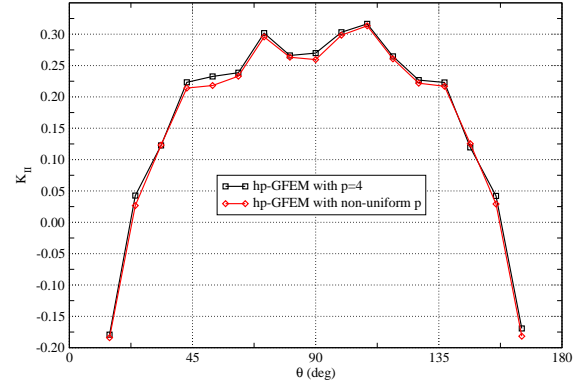
Figure 22: Hp-GFEM solution for non-uniform polynomial enrichment, discretization around crack surface and crack opening using integration elements as graphical elements.

Table 5: Number of degrees of freedom and strain energy for uniform $p = 4$ and non-uniform p .

Discretization	Number of dofs	Strain energy
Uniform $p = 4$	451230	6.31e-03
Non-uniform p	106128	6.01e-03



(a) K_I along crack front.



(b) K_{II} along crack front.

Figure 23: Extracted stress intensity factors along crack front.

6 Summary and Concluding Remarks

The present paper introduces an hp -version of the Generalized Finite Element Method (hp -GFEM) for three-dimensional fracture mechanics problems. Starting from arbitrarily coarse meshes, the proposed GFEM automatically creates strongly graded meshes along crack fronts and assigns suitable high order GFEM shape functions to nodes according to their geometric positions with respect to the crack front. High order enrichment functions are easily generated for the continuous and discontinuous parts of the solution using the partition of unity concept. Hierarchical polynomial enrichment, together with the partition of unity concept, adds enough flexibility to build non-uniform polynomial approximations without the need of transition elements.

The proposed hp -GFEM is able to deliver high order convergence rates in energy norm as well as in stress intensity factors. The robustness of the method is tested for three-dimensional problems with increasing level of complexity. The proposed hp -GFEM is robust enough to handle planar as well as non-planar crack surfaces embedded in non-trivial unstructured meshes. In all examples, the hp -GFEM shows to be robust and able to deliver high convergence rates in the solution and, consequently, the extracted stress intensity factors.

Another contribution of this paper is a procedure to handle non-planar three-dimensional crack surfaces. The procedure includes

- a high fidelity representation of crack surfaces that is completely independent of the volume GFEM mesh. Also, this technique is flexible enough to represent virtually any crack surface geometry;
- a Lagrangian description of the crack front. This feature is useful for updating the crack front in crack growth simulations and for providing base vectors of coordinate systems associated with crack front

enrichment functions (Cf. Figure 4);

- creation of integration sub-elements for computational elements that interact with non-planar crack surfaces. The numerical examples demonstrate that the resulting numerical integration is accurate and can be performed using standard quadrature rules. Moreover, it allows large elements far from the crack front which are suitable for p -enriched based approximations;
- ease of creation of crack surfaces in pre-existing meshes as illustrated in Section 5.4. This feature is suitable for simulations of industrial problems.

The proposed procedure is also suitable for crack propagation simulations. The representation of the crack surface does not have to be recomputed from scratch after each crack propagation step. The crack representation can be modified along its boundary without affecting its interior. This feature provides consistent representation of the crack surface for crack growth simulations. Details on the application of this approach to crack propagation problems will be presented elsewhere.

Acknowledgments: The partial support of this work by the Computational Science and Engineering program at the University of Illinois at Urbana-Champaign is gratefully acknowledged.

References

- [1] P.M.A. Areias and Ted Belytschko. Analysis of three-dimensional crack initiation and propagation using the extended finite element method. *International Journal for Numerical Methods in Engineering*, 63:760–788, 2005. [2](#), [3](#), [4](#), [10](#), [12](#), [13](#)
- [2] I. Babuška, U. Banerjee, and J.E. Osborn. Survey of meshless and generalized finite element methods: A unified approach. *Acta Numerica*, 12:1–125, May 2003. [6](#), [7](#)
- [3] I. Babuška, G. Caloz, and J.E. Osborn. Special finite element methods for a class of second order elliptic problems with rough coefficients. *SIAM Journal on Numerical Analysis*, 31(4):745–981, 1994. [7](#)
- [4] I. Babuška and J.M. Melenk. The partition of unity finite element method. *International Journal for Numerical Methods in Engineering*, 40:727–758, 1997. [2](#), [7](#)
- [5] G. I. Barenblatt. The mathematical theory of equilibrium cracks in brittle fracture. *Advances in Applied Mechanics*, 7:55–129, 1962. [13](#)
- [6] E. Béchet, H. Minnebo, N. Moës, and B. Burgardt. Improved implementation and robustness study of the x-fem for stress analysis around cracks. *International Journal for Numerical Methods in Engineering*, 64:1033–1056, 2005. [11](#)
- [7] T. Belytschko and T. Black. Elastic crack growth in finite elements with minimal remeshing. *International Journal for Numerical Methods in Engineering*, 45:601–620, 1999. [2](#)
- [8] T. Belytschko, Y. Krongauz, D. Organ, and M. Fleming. Meshless methods: An overview and recent developments. *Computer Methods in Applied Mechanics and Engineering*, 139:3–47, 1996. [7](#)
- [9] D.L. Chopp and N. Sukumar. Fatigue crack propagation of multiple coplanar cracks with the coupled extended finite element/fast marching method. *International Journal of Engineering Science*, 41:845–869, 2003. [2](#), [11](#), [12](#), [13](#)

- [10] M. de Berg, M. van Kreveld, M. Overmars, and O. Schwarkzopf. *Computational Geometry: Algorithms and Applications*. Springer, New York, NY, 2nd edition, 2001. [13](#), [14](#), [16](#)
- [11] C.A. Duarte, I. Babuška, and J.T. Oden. Generalized finite element methods for three dimensional structural mechanics problems. In S.N. Atluri and P.E. O'Donoghue, editors, *Modeling and Simulation Based Engineering*, volume I, pages 53–58. Tech Science Press, October 1998. Proceedings of the International Conference on Computational Engineering Science, Atlanta, GA, October 5-9, 1998. [2](#)
- [12] C.A. Duarte, I. Babuška, and J.T. Oden. Generalized finite element methods for three dimensional structural mechanics problems. *Computers and Structures*, 77:215–232, 2000. [2](#), [7](#), [8](#), [9](#), [10](#), [11](#), [20](#), [22](#)
- [13] C.A. Duarte, O.N. Hamzeh, T.J. Liszka, and W.W. Tworzydło. The element partition method for three-dimensional dynamic crack propagation. In *Fifth U.S. National Congress on Computational Mechanics*, page 297, Boulder, CO, August 1999. [2](#)
- [14] C.A. Duarte, O.N. Hamzeh, T.J. Liszka, and W.W. Tworzydło. Simulation of three-dimensional crack growth under impact loads using a partition of unity method. In *36th Annual Meeting of the Society of Engineering Science*, pages WB8–2, Austin, TX, October 1999. [2](#)
- [15] C.A. Duarte, O.N. Hamzeh, T.J. Liszka, and W.W. Tworzydło. A generalized finite element method for the simulation of three-dimensional dynamic crack propagation. *Computer Methods in Applied Mechanics and Engineering*, 190:2227–2262, 2001. [http://dx.doi.org/10.1016/S0045-7825\(00\)00233-4](http://dx.doi.org/10.1016/S0045-7825(00)00233-4). [2](#), [4](#), [9](#), [10](#), [11](#), [13](#)
- [16] C.A. Duarte, L.G. Reno, and A. Simone. A high-order generalized FEM for through-the-thickness branched cracks. *International Journal for Numerical Methods in Engineering*, 72(3):325–351, 2007. <http://dx.doi.org/10.1002/nme.2012>. [2](#), [4](#), [9](#), [12](#)
- [17] C.A.M. Duarte and J.T. Oden. An hp adaptive method using clouds. *Computer Methods in Applied Mechanics and Engineering*, 139:237–262, 1996. [7](#)
- [18] C.A.M. Duarte and J.T. Oden. Hp clouds—An hp meshless method. *Numerical Methods for Partial Differential Equations*, 12:673–705, 1996. [7](#)
- [19] M. Duflot. A study of the representation of cracks with level sets. *International Journal for Numerical Methods in Engineering*, 70:1261–1302, 2007. [4](#)
- [20] D. S. Dugdale. Yielding of steel sheets containing slits. *Journal of the Mechanics and Physics of Solids*, 8:100–108, 1960. [13](#)
- [21] T. C. Gasser and G.A. Holzapfel. 3D crack propagation in unreinforced concrete. A two-step algorithm for tracking 3D crack paths. *Computer Methods in Applied Mechanics and Engineering*, 195:5198–5219, 2006. [3](#), [4](#), [10](#), [12](#), [13](#)
- [22] T.C. Gasser and G.A. Holzapfel. Modeling 3D crack propagation in unreinforced concrete using PUFEM. *Computer Methods in Applied Mechanics and Engineering*, 194:2859–2896, 2005. [2](#), [3](#), [4](#), [10](#), [12](#), [13](#)

- [23] M. Gosz and B. Moran. An interaction integral method for computation of mixed-mode stress intensity factors along non-planar crack fronts in three dimensions. *Engineering Fracture Mechanics*, 69:299–319, 2002. [27](#), [28](#)
- [24] A. Gravouil, N. Moës, and T. Belytschko. Non-planar 3d crack growth by the extended finite element and level sets – Part II: Level set update. *International Journal for Numerical Methods in Engineering*, 53:2569–2586, 2002. [2](#), [4](#), [13](#)
- [25] M. Griebel and M.A. Schweitzer, editors. *Meshfree Methods for Partial Differential Equations II*, volume 43 of *Lecture Notes in Computational Science and Engineering*. Springer, 2005. [7](#)
- [26] P. Grisvard. *Singularities in Boundary Value Problems*. Research notes in Appl. Math. Springer-Verlag, New York, 1992. [9](#)
- [27] A. Hillerborg, M. Modeer, and P. E. Petersson. Analysis of crack formation and crack growth in concrete by means of fracture mechanics and finite elements. *Cement and Concrete Research*, 6:773–782, 1976. [13](#)
- [28] P. Keast. Moderate-degree tetrahedral quadrature formulas. *Computer Methods in Applied Mechanics and Engineering*, 55:339–348, 1986. [14](#)
- [29] P. Krysl and T. Belytschko. The element free Galerkin method for dynamic propagation of arbitrary 3-D cracks. *International Journal for Numerical Methods in Engineering*, 44:767–800, 1999. [4](#), [13](#)
- [30] P. Laborde, J. Pommier, Y. Renard, and M. Salaün. High-order extended finite element method for cracked domains. *International Journal for Numerical Methods in Engineering*, 64:354–381, 2005. [2](#), [11](#)
- [31] S. Li, M.E. Mear, and L. Xiao. Symmetric weak-form integral equation method for three-dimensional fracture analysis. *Computer Methods in Applied Mechanics and Engineering*, 151:435–459, 1998. [20](#), [22](#), [23](#)
- [32] G.R. Liu. *Mesh Free Methods: Moving Beyond the Finite Element Method*. CRC Press, July 2002. [7](#)
- [33] W.K. Liu, Y. Chen, S. Jun, J.S. Chen, T. Belytschko, C. Pan, R.A. Uras, and C.T. Chang. *Overview and Applications of the Reproducing Kernel Particle Methods*, volume 3 of *Archives in Computational Methods in Engineering: State of Art Reviews*. CIMNE, Barcelona, Spain, 1996. [7](#)
- [34] S. Mariani and U. Perego. Extended finite element method for quasi-brittle fracture. *International Journal for Numerical Methods in Engineering*, 58(1):103–126, 2003. [2](#)
- [35] J.M. Melenk and I. Babuška. The partition of unity finite element method: Basic theory and applications. *Computer Methods in Applied Mechanics and Engineering*, 139:289–314, 1996. [7](#)
- [36] J. Mergheim, E. Kuhl, and P. Steinmann. Towards the algorithmic treatment of 3d strong discontinuities. *Communications in Numerical Methods in Engineering*, 23:97–108, 2007. [2](#), [3](#)
- [37] N. Moes, J. Dolbow, and T. Belytschko. A finite element method for crack growth without remeshing. *International Journal for Numerical Methods in Engineering*, 46:131–150, 1999. [2](#), [13](#), [26](#)

- [38] N. Moës, A. Gravouil, and T. Belytschko. Non-planar 3D crack growth by the extended finite element and level sets – Part I: Mechanical model. *International Journal for Numerical Methods in Engineering*, 53:2549–2568, 2002. [2](#), [4](#), [9](#), [11](#), [12](#), [13](#)
- [39] S.A. Nazarov and B.A. Plamenevsky. *Elliptic Problems in Domains with Piecewise Smooth Boundaries*, volume 13 of *De Gruyter Expositions in Mathematics*. Walter de Gruyter, Berlin, 1994. [9](#)
- [40] J.T. Oden and C.A. Duarte. Chapter: Clouds, Cracks and FEM’s. In B.D. Reddy, editor, *Recent Developments in Computational and Applied Mechanics*, pages 302–321, Barcelona, Spain, 1997. International Center for Numerical Methods in Engineering, CIMNE. [10](#)
- [41] J.T. Oden, C.A. Duarte, and O.C. Zienkiewicz. A new cloud-based *hp* finite element method. *Computer Methods in Applied Mechanics and Engineering*, 153:117–126, 1998. [2](#), [7](#), [8](#), [23](#)
- [42] J.T. Oden and C.A.M. Duarte. Chapter: Solution of singular problems using *hp* clouds. In J.R. Whiteman, editor, *The Mathematics of Finite Elements and Applications– Highlights 1996*, pages 35–54, New York, NY, 1997. John Wiley & Sons. [10](#)
- [43] J. Oliver, A.E. Huespe, E. Samaniego, and E.W.V. Chaves. Continuum approach to the numerical simulation of material failure in concrete. *International Journal for Numerical and Analytical Methods in Geomechanics*, 28(7–8):609–632, 2004. [2](#)
- [44] J.P. Pereira and C.A. Duarte. Extraction of stress intensity factors from generalized finite element solutions. *Engineering Analysis with Boundary Elements*, 29:397–413, 2005. [20](#), [27](#)
- [45] B. Prabel, A. Combescure, A. Gravouil, and S. Marie. Level set X-FEM non-matching meshes: Application to dynamic crack propagation in elasticplastic media. *International Journal for Numerical Methods in Engineering*, 69:1553–1569, 2007. [13](#)
- [46] J. C. Raju, I. S. Newman Jr. Three dimensional finite-element analysis of finite-thickness fracture specimens. Report TN D-8414, NASA - Langley Research Center, Hampton, VA, May 1977. pp. 1-40. [22](#), [23](#)
- [47] J.A. Sethian. *Level Set Methods and Fast Marching Methods Evolving Interfaces in Computational Geometry, Fluid Mechanics, Computer Vision, and Materials Science*. Cambridge Monograph on Applied and Computational Mathematics. Cambridge University Press, 1999. [4](#)
- [48] A. Simone. Partition of unity-based discontinuous elements for interface phenomena: Computational issues. *Communications in Numerical Methods in Engineering*, 20:465–478, 2004. [9](#), [13](#)
- [49] A. Simone, C.A. Duarte, and E. van der Giessen. A generalized finite element method for polycrystals with discontinuous grain boundaries. *International Journal for Numerical Methods in Engineering*, 67(8):1122–1145, 2006. <http://dx.doi.org/10.1002/nme.1658>. [9](#)
- [50] F.L. Stazi, E. Budyn, J. Chessa, and T. Belytschko. An extended finite element method with higher-order elements for curved cracks. *Computational Mechanics*, 31:38–48, 2003. [2](#)
- [51] T. Strouboulis, K. Copps, and I. Babuška. The generalized finite element method. *Computer Methods in Applied Mechanics and Engineering*, 190:4081–4193, 2001. [2](#), [7](#)

- [52] N. Sukumar, D.L. Chopp, and B. Moran. Extended finite element method and fast marching method for three-dimensional fatigue crack propagation. *Engineering Fracture Mechanics*, 70:29–48, 2003. [2](#), [11](#), [12](#), [13](#)
- [53] N. Sukumar, N. Moes, B. Moran, and T. Belytschko. Extended finite element method for three-dimensional crack modelling. *International Journal for Numerical Methods in Engineering*, 48(11):1549–1570, 2000. [2](#), [4](#), [9](#), [11](#), [12](#), [13](#), [23](#), [26](#)
- [54] N. Sukumar and J.-H. Prevost. Modeling quasi-static crack growth with the extended finite element method Part I: Computer implementation. *International Journal of Solids and Structures*, 40:7513–7537, 2003. [13](#)
- [55] B. Szabo and I. Babuška. *Finite Element Analysis*. John Wiley and Sons, New York, 1991. [2](#), [3](#), [6](#), [10](#), [20](#), [23](#), [27](#)
- [56] B. A. Szabo and I. Babuška. Computation of the amplitude of stress singular terms for cracks and reentrant corners. In T.A. Cruse, editor, *Fracture Mechanics: Nineteenth Symposium, ASTM STP 969*, pages 101–124, Southwest Research Institute, San Antonio, TX, 1988. [20](#), [27](#)
- [57] H. Tada, P. Paris, and G. Irwin. *The Stress Analysis of Cracks Handbook*. ASME Press, New York, 3rd edition, 2000. [25](#)
- [58] R.L. Taylor, O.C. Zienkiewicz, and E. Onate. A hierarchical finite element method based on the partition of unity. *Computer Methods in Applied Mechanics and Engineering*, 152:73–84, 1998. [2](#)
- [59] Lloyd N. Trefethen and David Bau III. *Numerical Linear Algebra*. SIAM, Philadelphia, PA, 1997. [17](#)
- [60] G.N. Wells and L.J. Sluys. A new method for modeling cohesive cracks using finite elements. *International Journal for Numerical Methods in Engineering*, 50:2667–2682, 2001. [2](#), [9](#), [12](#), [13](#)